Combustion and Flame 270 (2024) 113689

Contents lists available at ScienceDirect

Combustion and Flame

journal homepage: www.sciencedirect.com/journal/combustion-and-flame

Structure-reactivity correlations for reactions between H/D atoms with selected ethers: Reaction-rate coefficients from direct shock-tube measurements and transition-state theory

F. Werner [a,b,*], C. Naumann [a], M. Braun-Unkhoff [a,1], T. Methling [a], C. Schulz [c], U. Riedel [b], S. Peukert [c]

[a] German Aerospace Center (DLR), Institute of Combustion Technology, Stuttgart, Germany
[b] German Aerospace Center (DLR), Institute of Low-Carbon Industrial Processes, Cottbus, Germany
[c] Institute for Energy and Materials Processes – Reactive Fluids, University of Duisburg-Essen, Duisburg, Germany

ARTICLE INFO

Keywords:
H-atom abstraction from ethers
Shock tube
H-ARAS
D-ARAS
Dual ARAS
Transition-state theory
Structure-reactivity relationship

ABSTRACT

Shock-tube experiments at elevated pressures between 2.0 and 2.7 bar were carried out to study H-atom abstractions between D atoms and selected ether compounds: dimethyl ether (DME), diethyl ether (DEE), dimethoxymethane (DMM), and methyl propyl ether (MPE). D-atom resonance absorption spectrometry (D-ARAS) behind reflected shock waves was used to monitor the consumption of D atoms. To study the bimolecular reactions between D atoms and the specific ether, gas mixtures of the selected ether compound and C_2D_5I diluted in argon (bath gas) were prepared; C_2D_5I was used as a precursor for D atoms. This innovative approach using Dual ARAS (D-ARAS and H-ARAS) allows the distinct detection of precursor decay followed by H-atom abstraction reactions and ether decay followed by H-atom release. For the study of the reaction D + DME → HD + products, the experiments covered a temperature range of 940–1050 K; for the reaction D + DEE → HD + products, the temperature range was 980–1260 K; for the reaction D + DMM → HD + products, the temperature range was 930–1300 K; and for the reaction D + MPE → HD + products, the temperature spans a range of 1000–1350 K. Experimentally determined rate coefficients have been expressed by the following Arrhenius equations:

$k_{total(D+DME)}(T) = 1.9\times10^{-10}$ exp (−31.4 kJ/mol / RT) cm^{3}s^{-1},
$k_{total(D+DEE)}(T) = 1.7\times10^{-10}$ exp (−22.4 kJ/mol / RT) cm^{3}s^{-1},
$k_{total(D+DMM)}(T) = 2.7\times10^{-10}$ exp (−27.3 kJ/mol / RT) cm^{3}s^{-1},
and $k_{total(D+MPE)}(T) = 5.1\times10^{-10}$ exp (−31.5 kJ/mol / RT) cm^{3}s^{-1}.

The experimental results show an uncertainty of ±30 % and were supplemented by transition-state theory (TST) calculations based on molecular properties and energies from computations at the G4 level of theory. TST computations were conducted for H-atom abstraction from various types of primary and secondary carbon bonds. Bond-specific reaction rate-coefficient expressions were derived from theory and compared with experimental results to establish correlations between molecular structure and reactivity.

1. Introduction

Oxygenated hydrocarbons are important as both neat biomass-based fuels (biofuels) and as fuel additives. They are becoming increasingly relevant as sustainable fuels due to their production by electrochemical and catalytic processes (e-fuels). In addition to alcohols, ethers, which also belong to the group of oxygenated hydrocarbons, are used as additives and components in synthetic fuels. The simplest ether is dimethyl ether (CH_3OCH_3, DME). DME is produced on a large scale from synthesis gas (CO and H_2) and can be used, for example, as a fuel in stationary gas turbines, as a substitute for liquid gas, and as a feedstock for chemical production [1]. A series of reaction kinetics studies [2-4] have investigated the pyrolysis and oxidation of DME, highlighting its importance. Diethyl ether ($C_2H_5OC_2H_5$, DEE) has also been used as a fuel additive, in addition to DME. Yasunaga *et al.* [5] systematically investigated the ignition properties of DEE. Oxymethylene ethers (OMEs) are a group of

* Corresponding author at: DLR Stuttgart.
E-mail address: fabienne.werner@dlr.de (F. Werner).
[1] retired

https://doi.org/10.1016/j.combustflame.2024.113689
Received 22 February 2024; Received in revised form 19 August 2024; Accepted 20 August 2024
Available online 19 September 2024

ether compounds that can serve as both additive and as fuel. They have the general chemical structure CH_3–O– $(CH_2$–O$)_n$–CH_3 and can be produced from methanol in several steps. OMEs are an interesting energy storage medium that can ultimately be produced from electrolytically generated (green) hydrogen [6,7]. Since dimethoxymethane (CH_3–O–CH_2–O–CH_3, DMM) is considered a model component for the group of OMEs, several theory and experimental kinetics studies on the pyrolysis and oxidation of DMM have been reported [8-16].

In combustion modeling, reaction mechanisms use elementary reactions that are grouped by reaction classes. These include in particular H-atom abstractions by small and reactive radicals, *i.e.,* reactions of the type OH/O/H/CH_3 + RH ⇋ H_2O/OH/H_2/CH_4 + $R^\bullet$. In combustion processes, H-atom abstractions play a crucial role in the oxidation of hydrocarbons and in the oxidation of oxygen-containing species, such as ethers. Mechanisms developed to simulate ignition delay times of DME/O_2 gas mixtures have identified H-atom abstractions H/OH + DME ⇋ H_2/H_2O + $CH_3OCH_2^\bullet$ as having large sensitivities [17].

In the past 30 years, the development of reaction mechanisms for combustion modeling has been aided by devising structure-reactivity relationships or rate-rule approximations for important reaction classes such as H-atom abstractions. In the 1980s and 1990s, Bott, Koffend, and Cohen conducted shock-tube experiments at $T \approx 1200$ K to determine the rate coefficients for reactions between OH radicals and linear and branched hydrocarbons; thus, they developed the first rate-rule based approximations for $T > 1000$ K [18-20]. Sivaramakrishnan *et al.* expanded the temperature range of the Cohen *et al.* experiments to 800-1320 K. They interpreted the measured data with transition-state theory (TST) computations based on modern quantum-chemical methods and generalized them to rate-rules based on the principle of group additivity [21,22]. In addition to H-atom abstractions by OH radicals, structure-reactivity relationships have been developed for reactions between H atoms and hydrocarbons, to some extent, by Carstensen and Dean [23], by Sivaramakrishnan and Michael [24], and by Peukert *et al.* [25]. H-atom abstraction by H atoms is still a reaction class where kinetics data from direct measurements is scarce, particularly at high temperatures for even small to mid-size ether compounds. This lack of urgently needed data has motivated the present work on reactions between H atoms and different ether compounds following the approach of a combined experimental, modeling, and theoretical study.

Ogura *et al.* [26] provide the most systematic theory-based approach for deriving structure-reactivity relationships in H-atom abstractions in H/OH + (open-chain) ether compound reactions. They computed reaction rate coefficients for abstractions in which the abstracted H atoms are attached to C atoms in close proximity to the O atom of an ether molecule. Preliminary rate-rule approximations were determined from these computations. These rate-rules pertain to the following groups in ether compounds: CH_3(O), CH_2(O), and CH(O). These groups indicate primary, secondary, and tertiary C–H bonds, respectively, in the vicinity of the O atom.

In this work, we also intend to derive structure–reactivity correlations for H-atom abstractions from different types of C–H bonds in ether compounds. In addition to quantum-chemical computations and TST, we also directly measure overall abstraction rate coefficients using atomic resonance absorption spectrometry (ARAS) to measure deuterium atoms (D-ARAS) at 121.534 nm.

For the experimental determination of rate coefficients of H + ether reactions, the highly sensitive H-ARAS measurement technique can in principle be used, by which the H-atom concentration $[H]_t$ is measured time-resolved by resonance absorption of Lyman-α radiation at 121.568 nm. However, it should be noted that H-atom abstractions produce ether radicals that decompose rapidly to eventually release H atoms. The $[H]_t$ profile is affected not only by the bimolecular reactions in focus but also by subsequent reactions. This poses a challenge in interpreting the signal and determining reaction rate coefficients. This issue can be resolved by substituting hydrogen (H) with deuterium (D). Using D atoms for reactions are a suitable analogy to measurements with H atoms because at temperatures above 1000 K, the kinetic isotope effect becomes very small, *i.e.,* $k_H/k_D \approx 1.1$ [24,27,28].

For these reasons, H-ARAS and D-ARAS have been applied simultaneously in shock-tube experiments. This strategy also allows testing the performance of reaction mechanisms including the DLR Concise [29], which was developed at the DLR Institute of Combustion Technology [29]. By measuring the D atom consumption and the H atom formation simultaneously, we can determine the overall H-atom abstraction rate coefficients (by D-ARAS) and obtain information about the ongoing secondary reactions related to the decomposition of ether radicals generated by H-atom abstractions (H-ARAS).

This work investigates H-atom abstractions by H/D atoms on the four compounds DMM, DME, DEE, and methyl propyl ether (MPE) using experiments and theory. These four compounds contain different types of primary and secondary C–H bonds: P_1, P_0, S_{0a}, S_{0b}, S_1. Depending on the molecular structure of these ethers, the different groups of C–H bonds exhibit energy barriers that vary by several kJ/mol. As a result, they have a different weighted contribution to overall H-atom abstraction rate coefficients. By combining experiment and theory, we aim to get detailed information of structure-reactivity correlations between different primary and secondary C–H bond types in open-chain ether molecules, as well as their reactivity in terms of H-atom abstraction rate coefficients. Hereby, the comparison of different types of C-H bonds within one ether and C-H bonds of one type but in different ethers is drawn. In total, four ethers containing five different C-H bond types (see Fig. 1) are considered.

2. Experimental methods

2.1. Shock-tube apparatus

The experiments shown in this work were conducted in a stainless-steel shock tube used in previous research [30] but with a new measurement setup. Driver (length: 6.33 m) and driven (length: 4.09 m) sections have an inner diameter of 7.2 cm and were separated by an 80 μm thick aluminum diaphragm. Helium (Linde) ≥ 99 % was used as driver gas. The driver section was pressurized until diaphragm rupture, generating the shock wave in the driven section. The low-pressure section contained the reactive mixture highly diluted in argon (Linde) ≥ 99 %. To calculate the post-shock conditions, the one-dimensional gas dynamic Rankine-Hugoniot equations were solved, which required the pre-shock conditions (mixture, initial temperature, and pressure) as well as the incident shock wave velocity that was measured by four thin-film platinum heat transfer sensors.

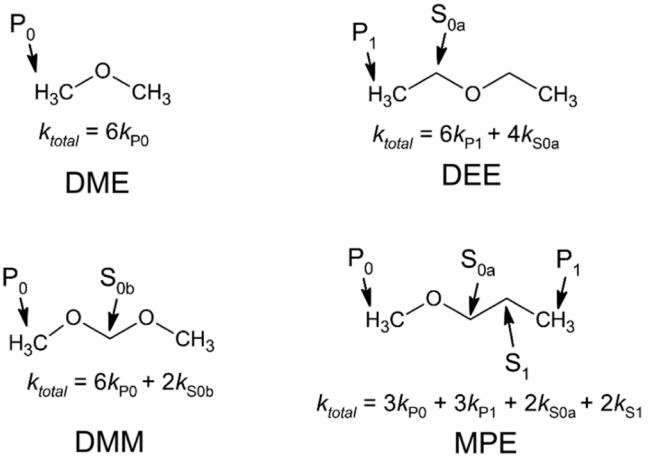

Fig. 1. Ether compounds studied and considered for analyzing structure–reactivity correlations for H-atom abstractions. C–H bonds are classified by groups such as P_0, P_1, S_{0a}, S_{0b}, and S_1.

Table 1
Summary of mixture concentrations.

Reaction	C_2D_5I decay	DME + D	DEE + D	DMM + D	MPE + D
Detection Method	D-ARAS	D-ARAS	D/H dual ARAS	D/H dual ARAS	D/H dual ARAS
$[C_2D_5I]_0$ in ppm	5.00; 2.50; 1.25	5.00; 2.50; 1.25	5.00; 2.50; 1.25	5.00; 2.50; 1.25	5.00; 2.50; 1.25
[oxygenated hydrocarbon]$_0$ in ppm	-	25.00; 12.50; 6.25	25.00; 12.50; 6.25	25.00; 12.50; 6.25	25.00; 12.50; 6.25

2.2. ARAS Detection

The measurement plane was located 0.5 cm before the incident shock wave reflection plane. The reaction progress behind the reflected shock wave was investigated with time-resolved D- and H-ARAS. The source of the vacuum-ultraviolet light was a microwave discharge lamp operated with a lamp gas containing (1.00±0.02) % H_2 or (1.00±0.02) % D_2 in He (LINDE), leading to radiation at the Lyman-α wavelength, with λ = 121.568 nm for absorption by H atoms and λ = 121.534 nm for absorption by Datoms, respectively. The light was passed through the shock tube via MgF_2 windows and detected by a solar-blind photomultiplier (Electron Tubes PMT 9403B). Spectral selectivity was ensured by a Lyman-α interference filter (Acton Research, FWHM = 10 nm) in combination with a constant flow of oxygen (purity ≥ 99.95 %, Linde AG). Spatial resolution was enhanced by using slits of 1 mm width in front of the entry and exit windows. Signals emerging from the photomultiplier were amplified, bandwidth limited to 1 MHz@12dB/oct. by an SR560 amplifier (Stanford Research Systems), and recorded with a digital storage oscilloscope (GEN2tB/GN815, HBK GmbH) at a sampling rate of 1 MHz that was triggered through a piezoelectric pressure transducer (PCB 113B21) located at the end plate.

To convert the measured absorption profiles into concentration profiles of H- or D atoms a calibration of the ARAS setup was mandatory because of the self-inverted line shapes of the emitted light. Therefore, mixtures of H_2/N_2O (AGA Gas GmbH) containing N_2O (2.0 ± 0.1) ppm and H_2 (207 ± 10) ppm, and D_2/N_2O (Linde AG) containing N_2O (2.28 ± 0.12) ppm and D_2 (191 ± 4) ppm, diluted in highly purified argon were used for the calibration experiments.

Below T = 2000 K, the increase of the detected H-radicals is dynamical and can be used to form a correlation with the respective absorber concentration calculated by modeling using the reaction mechanism of Glarborg *et al.* [31] with extensions related to the D_2 kinetics reported by Pamidimukkala and Skinner [32]. Eventually, the absorption-absorber correlation can be fitted using a modified Lambert-Beer equation:

$$A = 1 - \exp\left(-l \times s^{(3n-1)} \times [\mathrm{X}]^n\right) \quad (1)$$

where A is the absorption and l the optical path length in cm; n is a dimensionless exponent. For n = 1, Eq. (1) reduces to the Lambert-Beer law of absorption, where s^2 represents the absorption cross section in units of cm^2; [X] is the number density of the absorbing species in cm^{-3n}; s and n are fitting parameters providing the correlation $f(A)$ = [X].

Non-resonant absorption cross sections of DMM, DME, DEE, and MPE were determined by the increase of light absorption linked to the incident shock wave accompanied by an increasing density of the tested gas.

Measurements of the decay of C_2D_5I and the subsequent reaction of D with DME were obtained using only one ARAS beam line. All other measurements were performed with a Dual ARAS setup allowing the detection of D- and H-radicals simultaneously.

2.3. Reactant mixtures

Test mixtures were prepared in a stainless-steel vessel heated to 393 K. Before filling, the vessel was flushed with argon and evacuated to pressures down to approx. 1×10^{-6} mbar. Gas mixtures were prepared in the concentrations given in Table 1 using the partial pressure method and were allowed to homogenized overnight. The accuracy of the concentration of the mixtures as well as their stability and purity were verified using gas chromatographic analysis with flame ionization as detection method (GC-FID).

The purity of the gases and of the chemicals used was as follows: C_2D_5I (Sigma Aldrich) ≥ 99 %, DME (Linde) 99.9 %, DEE (Bernd Kraft) 99.5 %, DMM (Roth) 99.9 %, Ar (Linde) ≥ 99.9999 %, and He (Linde) ≥ 99.996 %. H-ARAS and D-ARAS absorption signals were calibrated against measurements with gas mixtures (AGA Gas GmbH) containing N_2O (2.0 ± 0.10 ppm), H_2 (207 ± 10 ppm), rest Ar.

3. Theory

Fig. 1 shows the molecules studied in this work, with each of these compounds having certain structural units that can be classified into groups. The classification is similar to the next-nearest-neighbor configuration scheme proposed by Cohen [33].

The groups labeled P and S refer to primary and secondary C–H bonds. These groups are further differentiated: P_0 refers to primary C–H bonds in CH_3 moieties bonded adjacent to an O atom and P_1 refers to C–H bonds in terminal CH_3 moieties of linear ethers, which are placed next to a CH_2 fragment. The group S_{0a} refers to secondary C–H bonds whose C atom is located next to an O atom, while in the group S_{0b} the C atom of such secondary C–H bonds is connected to two O atoms. The S_{0b} group is therefore characteristic for the compound class of OMEs. A further internal differentiation is made by the S_1 group: S_1 characterizes C–H bonds whose C atom is located between a primary and secondary C atom.

Due to minor differences in bond–dissociation energies by a few kJ/mol, abstractions from C–H bonds assigned to different groups exhibit slightly different energy barriers. Thus, abstractions at C–H bonds from different groups have slightly different weighted contributions to the overall H-atom abstraction rate coefficient, k_{total}. DMM, for example (see Fig. 1), has six C–H bonds of type P_0 and two C–H bonds of type S_{0b}. Accordingly, k_{total} should result in $6\times k_{P1} + 2\times k_{S0b}$.

From the present D-ARAS shock-tube experiments, only overall H-atom abstraction rate coefficients can be measured. To interpret the experimentally determined values for k_{total}, *ab initio* transition-state theory (TST) calculations have been conducted. C–H bond type specific H-atom abstraction rate coefficients have been computed applying TST. Theory-based k_{total} values were obtained by adding up the bond-specific rate-coefficient values, which were then compared with the measured k_{total} data.

TST calculations were based on molecular rovibrational properties and energetics of the minima and transition states obtained by quantum-chemical computations using the G4 composite method [34] implemented in GAUSSIAN 16 [35]. Cartesian coordinates and vibrational frequencies of reactants, transition states, and products are provided in the Supplementary Material (SM).

Composite methods such as G4 became a popular choice for the development of combustion reaction mechanisms since their performance has been benchmarked in great detail against the Active Thermochemical Tables (ATcT) [36,37]. The G4 method has been previously successfully applied to support experimental results by means of theory in various kinetics studies [38,39].

Within the G4 method, geometry optimizations and vibrational frequency analyses are carried out at the B3LYP/6-31G(2df,p) level of theory and the computed frequency values are scaled by 0.99 for the zero-point energy. Torsional motions of CH_3 moieties were treated as

hindered rotations. For such hindered rotations, energy barriers were obtained from relaxed potential energy surface (PES) scans at the B3LYP/6-31G(2df,p) level of theory with dihedral angles used as coordinates for the scans.

H-atom abstraction rate coefficients from TST of reactions between H and D atoms with ether molecules were calculated using the KiSThelP code [40]. The one-dimensional asymmetric Eckart correction was applied to account for tunneling. Hindered rotations were treated by using the hindered-rotor density-of-states method implemented in the KiSThelP program [41].

4. Modeling

By utilizing an adapted version of the SENKIN code from the CHEMKIN II program suite [42], the experimental D- and H-atom concentration profiles were modeled. Using the modified Lambert-Beer law (Eq. 1), computed concentration profiles were converted into absorption profiles which were then compared to experimentally measured absorption profiles. The experimentally determined non-resonant absorption cross sections were implemented to correctly model absorption caused by ethers present in the reacting mixture.

For each reaction system consisting of C_2D_5I and ether besides the diluent (Ar), a rate-of-progress (ROP) analysis [43] was performed to reveal potentially competitive reactions between deuterium atoms and decomposition products of the respective ether. We would like to highlight, that the rate-of-progress variable q_i is different from the often-used production rate ω_k and is defined as:

$$q_i = k_{f_i} \prod_{k=1}^{K} [X_k]^{\nu(k_i)'} - k_{r_i} \prod_{k=1}^{K} [X_k]^{\nu(k_i)''} \quad (2)$$

where k_{fi} and k_{ri} are the forward and reverse rate constants of the i-th reaction, and $[X_k]$ is the molar concentration of the k-th species; $\nu(k_i)$ represents the associated stoichiometric coefficient as integer number [43]. Here, only reactions including the species H or D are considered revealing the paths of production and consumption of this species. All shown ROP trends are normalized by the sum over ROP of all contributing reactions for each time step, allowing a comparison between the different reaction pathways.

With T increasing, ether decomposition reactions gain importance and must be included. To compare measured and calculated D-atom absorption, branching ratios (BR) of different reactions were kept constant, and the overall reaction rate coefficient k_{total}(D + ether) was adjusted.

For modeling the species decomposition of the systems studied in the present work, several reaction models have been used. Using the DLR Concise mechanism [29], H-atom abstraction reactions in DMM and DME/ were modeled. For modeling the D+DEE reaction, the mechanism published by Yasunaga *et al.* in 2010 has been implemented [5]. MPE was modeled using a mechanism constructed with the Reaction Mechanism Generator software (RMG), published by Johnson *et al.* in 2021 [44]. Within the Supplemental Materials a table can be found showing all used mechanisms regarding the individual reactive system as well as an overview of all reaction-rate coefficients presented in the scope of the present work.

Simultaneously to the D-ARAS measurements, H-atom absorption profiles were recorded by H-ARAS. After adjusting the overall rate coefficients of ether+D reactions in the first step, the H-atom absorption profiles were simulated to check whether the applied reaction mechanisms are able to capture the formation of H atoms, which result from the decomposition of initially formed ether radials and further subsequent reactions. However, re-analyzing reaction pathways of subsequent reactions of ether radicals is beyond the scope of this work and was therefore not considered in the present work.

The workflow behind the results shown is visualized in Fig. 2. ARAS measurements are used to acquire absorption profiles that are modeled using existing kinetics mechanisms. ROP analysis of these mechanisms provide information about potential competitive reactions. Adjusting the reaction rate of k_{total}(ether+D) provides the experimentally determined reaction-rate coefficients which can be compared with the TST calculations described and literature values presented. The branching ratios of different H-atom abstraction reactions within a molecule were kept constant because the measurements did not allow differentiation between different C–H sites.

5. Results

In this section, reaction rate coefficients gathered from experimental

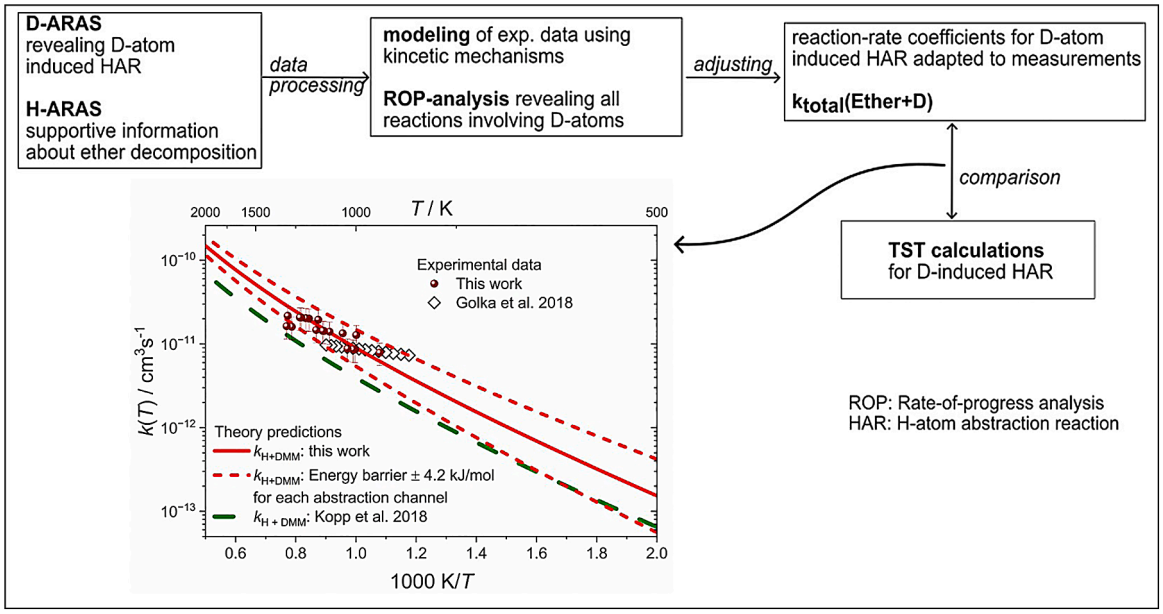

Fig. 2. Workflow that includes TST computations and experiments. Utilizing kinetics mechanisms, measured absorption profiles are modeled. Calculation and absorption profiles are matched by modifying (ether+D) reaction rate coefficients following the identification of potentially competitive reactions. The final step compares these values to TST calculations carried out within the purview of this work and values found in the literature.

measurements and TST calculations are presented and put into context with existing literature values. Similar to comparable studies, the uncertainty of experimentally determined reaction rate coefficients is estimated to be 30 % (see Figs. 3,5,8,11,14) [51]. First, deuterated ethyl iodide was kinetically described to allow a reliable prediction of its reaction system consisting the reactions (R1) to (R5) and therefore the production of D atoms. This thereby well characterized reaction system was used later on for investigating H-atom abstraction reactions in the mentioned linear ethers. Non-resonant absorption cross-sections of each ether had to be determined to allow accurate modeling of experimental absorption profiles. Concentrations of the test gas mixtures were chosen as presented in Table 1 to realize a surplus of ether in comparison to C_2D_5I promoting the reaction of D + ether. A higher ether concentration was not useful due to the associated increase in non-resonant absorption, which would have limited the absorption range between non-resonant absorption and saturation.

A list of all described reaction rate coefficients can be found in the Supplementary Material. Due to the design of the shock tube, diffusion effects are negligible within the reaction times shown.

5.1. Decomposition of deuterated ethyl iodide (C_2D_5I)

The reaction mechanism of ethyl iodide in its non-isotopic form (C_2H_5I) has been investigated in numerous studies [45-51] and can be essentially described by only five reactions, (R1) – (R5).

$$C_2H_5I \rightleftharpoons C_2H_5 + I \quad (R1)$$

$$C_2H_5 + M \rightleftharpoons C_2H_4 + H + M \quad (R2)$$

$$C_2H_5I \rightleftharpoons C_2H_4 + HI \quad (R3)$$

$$H + HI \rightleftharpoons H_2 + I \quad (R4)$$

$$C_2H_5I + H \rightleftharpoons C_2H_5 + HI \quad (R5)$$

(R1) represents the C–I bond fission followed by (R2), the fast decomposition of the ethyl radical yielding ethene and H atoms. The 1,2-HI elimination reaction (R3) competes with (R1), but has been shown to be less relevant [51]. To describe the formation of H atoms, the branching ratio $\Phi_1 = k_{R1}/(k_{R1} + k_{R3})$ is used. Reported values range from 0.87 ± 0.11 [47] to a maximum of 0.96 [48]. Here, in the present work, k_1 was determined using the relation Eq. (3):

$$k_{R1} = \frac{1}{[C_2D_5I]_0} \frac{d[D]}{dt} \text{ for } t \to 0 \quad (3)$$

as shown in Fig. 3.

Since (R1), followed by (R2), prevails over (R3), the initial concentration increase is caused by the C–I bond fission and the subsequent decay of C_2D_5 radicals. In this way, reaction rate coefficients for temperatures between 930 and 1100 K were obtained. At $T < 930$ K, the increase in D atom concentration is too slow to be detected due to the low rate of reaction (R1). At $T > 1200$ K, the C_2D_5I decomposition is too fast compared to the spatial resolution of the ARAS-detection system. The reaction rate coefficients obtained from a linear fit are shown in the Arrhenius diagram in Fig. 2 (right). The resulting Arrhenius expression is:

$$k_{R1}(T)/s^{-1} = 9.9\times10^{11} \exp(-167.7 \text{ kJ/mol} / RT). \quad (4)$$

The best fit between simulated and measured concentrations is achieved for $\Phi_1 = k_{R1}/(k_{R1} + k_{R3}) = 0.92$. The reaction rates for (R2), (R4), and (R5) were adapted from Bentz *et al.* [51]. For achieving the best fit to the experimental profiles at reaction times beyond 500 µs, it was necessary to adjust (R4) and (R5) by a factor of 0.75. All reaction coefficients of this radical precursor subsystem derived herein remain unchanged throughout the further investigation.

5.2. Non-resonant absorption cross-sections

All ethers examined in this work showed non-resonant absorption at the Lyman-α wavelength. The absorption cross-section for each reactant was determined at non-reactive conditions for temperatures below 950 K. Cross-sections determined are:

$\sigma_{DME} = (2.0 \pm 0.2)\times10^{-17}$ cm^2, $\sigma_{DMM} = (5.0 \pm 0.2)\times10^{-17}$ cm^2, $\sigma_{DEE} = (4.0 \pm 0.2)\times10^{-17}$ cm^2, and $\sigma_{MPE} = (6.8 \pm 0.9)\times10^{-17}$ cm^2.

The effect of non-resonant absorption can be observed in the absorption profiles shown as, e.g., in Fig. 7 (left). The initial increase in absorption can be explained by the compression caused by the incident shock wave. The temperature-dependent deviations within the experimental conditions shown are within the range of uncertainty.

5.3. H/D + DME

As all investigated species, DME was introduced into a mixture with C_2D_5I in argon at a ratio of 5:1. DME has only one type of a C–H bond, *i.e.,* P_0, that can react with D atoms by H-atom abstraction:

$$D^\bullet + CH_3OCH_3 \rightleftharpoons HD + CH_3OCH_2^\bullet \quad (R6a)$$

TST computations have been conducted for H-atom abstractions by D and H atoms. The H-atom abstraction analogue to (R6a) considering H atoms as reaction partner is designated as (R6b):

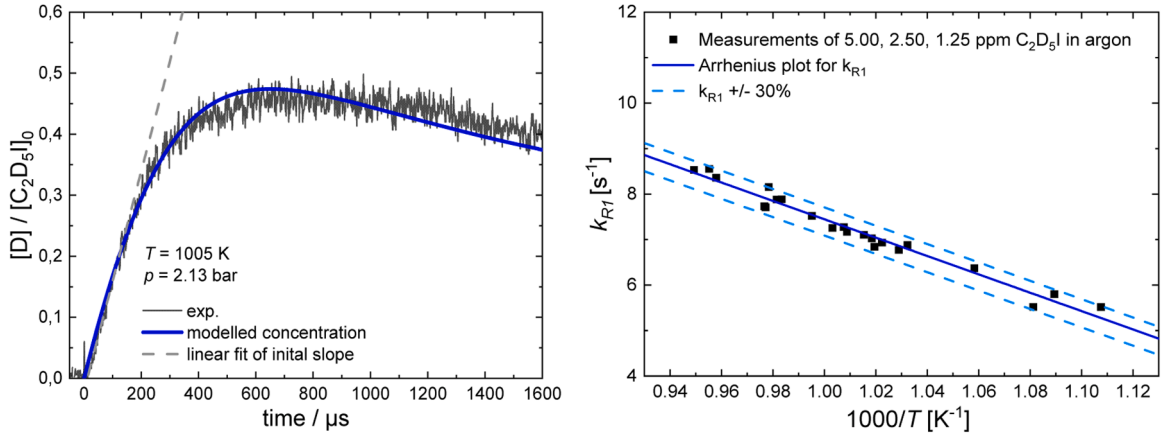

Fig. 3. Left: Measured $[D]_t$ profile obtained during the pyrolysis of 2.50 ppm C_2D_5I in argon at $T_5 = 1005$ K and $p_5 = 2.13$ bar compared with simulation (blue solid curve); kinetic modeling based on initial slope fit (dashed line) and adjusted Arrhenius parameters from Bentz *et al.* [7]. Right: Arrhenius diagram showing experimentally determined reaction rate-coefficients k_1 (this work) at $[C_2D_5I]_0$ mole fractions of 5.00, 2.50, and 1.25 ppm in argon.

$H^{\bullet} + CH_3OCH_3 \leftrightharpoons H_2 + CH_3OCH_2^{\bullet}$. (R6b)

There are six primary C–H bonds of type P_0 (section 3). Fig. 3 shows measured D-atom absorption profiles (left) compared to modeled absorption and a D atom rate-of-progress analysis for the experiment at T_5 = 1006 K and p_5 = 2.55 bar (right). Initial increase of absorption is linked to an increase in $[D]_t$ caused by the previously described C_2D_5I decay. Declines found in of absorption profiles are linked to a decrease of $[D]_t$ caused by H-atom abstraction reactions consuming D atoms. All rate-of-progress plots shown here are normalized to the sum of all contributing reactions regarding the species D. Decomposition reactions of C_2D_5I are most dominant early in the experiment and result in an increase in D atoms, leading to an increase in the DME + D reaction rate of progress. Competing reactions to the H-atom abstraction reaction induced by D atoms cannot be found, as the exemplary reaction with CH_2O shows. The rate coefficient of this reaction is based on ARAS, IR emission, and CO-laser absorption measurements and thus proven TST calculations [52].

Modeling of the reactions at experimental conditions was performed using the DLR Concise mechanism [29] whereby the parameters for the H-atom abstraction reaction are based on calculations and measurements from [4,53]. As shown in Fig. 4 (left), there is good agreement between the mechanism predictions and our measurements. Our experimentally determined rate coefficients of reaction (R6a) and a comparison to other experimental data [2,50] and theoretical predictions based on TST calculations are shown in Fig. 5 (left).

Over the 930–1050 K temperature range (at pressures between 2.2–2.7 bar), our experimentally determined rate-coefficient data of reaction (R6a), $k_{R6a,exp}$, are represented by the following Arrhenius expression:

$$k_{R6a,exp}(T) = 1.9\times10^{-10} \exp(-31.4\ \text{kJ/mol} / RT)\ \text{cm}^3\text{s}^{-1} \quad (5)$$

On average, the uncertainty of estimated rate-coefficient data in this work, is estimated to be up to ± 30 %. The error bars on $k_{R6a,exp}$ data in Fig. 5 represent an estimated uncertainty of ±30 %. Based on *ab initio* computations on reaction (R6a) carried out in this work, the present TST prediction for $k(T)$ of H-atom abstraction per P_0 C–H bond, k_{P0}, is represented by the following expression:

$$k_{P0,DME}(T) = 3.7\times10^{-18} \times T^{2.20} \exp(-21.4\ \text{kJ/mol} / RT)\ \text{cm}^3\text{s}^{-1} \quad (6)$$

Note that Eq. (6) refers to H-atom abstraction by H atoms. Eq. (6) is valid for temperatures ranging between 500-2000 K. Multiplying $k_{P0,DME}$ with 6 (for six C–H bonds), results in $k_{R6b,TST}$ (Fig. 5). Please note that for all H-atom abstractions considered in this work, rate coefficients are computed per C–H bond type. The calculated rate-coefficient values for the respective C–H bond types, present in the ether molecule under investigation, are then added up to the total rate-coefficient value for the H-atom abstraction. The theory-based total rate-coefficient values obtained in this way are then compared to the experimental rate-coefficient data. Assuming an uncertainty in the predicted energy barrier of ±4.2 kJ/mol results in $k_{R6a,TST}$ data that are represented by the red dashed curves in Fig. 5 (left). Despite the deviation between the present theoretical data and the experimental results, the present $k_{R6a,exp}$ data are well within the uncertainty of this work's G4-based TST prediction. For all H-atom abstractions investigated in this work, rate-coefficient data have been computed for abstraction by H and D atoms. With respect to reactions (R6a) and (R6b), the right panel of Fig. 5 indicates that the kinetic-isotope effect is not related to the deviations between measurement and theory, *i.e.*, at temperatures above 1000 K, the kinetic-isotope effect $k_{R6a,TST}/k_{R6b,TST}$ is less than 1.03, and even between temperatures of 900 and 1000 K, the ratio $k_{R6a,TST}/k_{R6b,TST}$ is not exceeding 1.06. This applies to all H-atom abstractions studied in this work. Rate-coefficient data from D-ARAS experiments are an excellent approximation for H-atom abstractions by H atoms and are, therefore from now throughout this paper, compared to theoretical predictions related to abstractions by H atoms.

Here, it is assumed that the six P_0 C–H bonds are completely equivalent. DME is a molecule belonging to the C_{2v} point group, *i.e.*, there is an intramolecular mirror plane. Two C–H bonds are within this mirror plane (in-plane bonds; abbreviated as ip), whereas the other four C–H bonds are symmetrically out of this mirror plane (out-of-plane bonds; abbreviated as oop). Therefore, these P_0 bonds are not fully equivalent to each other, but in a previous study, Peukert *et al.* [54] showed that ip and oop C–H bonds in DME have no significant reactivity difference towards H-atom abstractions by H atoms. Therefore, the P_0 bonds in DME are treated as being equivalent.

At combustion relevant temperatures, (R6a) can be regarded as a well-characterized elementary reaction. Assuming similar experimental uncertainties for rate-coefficient data reported by Takahashi *et al.* [50] and Sivaramakrishnan *et al.* [2], the present experimental data are expected to be well within the uncertainties of other experimental data sets. Both data sets from refs. [2] and [50] were obtained from shock-tube experiments using the H-ARAS diagnostic; the reaction rate-coefficient values reported by Takahashi *et al.* represent direct measurements of k_{R6_b}, whereas the data obtained from Sivaramakrishnan *et al.* were obtained from modeling shock-tube experiments on DME decomposition. The G4-based TST theory prediction agrees well with all available experimental high-temperature rate-coefficient values on (R6b) and there is also a very good agreement with the prediction obtained by a reaction rate-rule expression provided by Ogura *et al.* [26], who conducted G3(MP2)//B3LYP-based TST computations to also predict H-atom abstraction rate coefficients per C–H

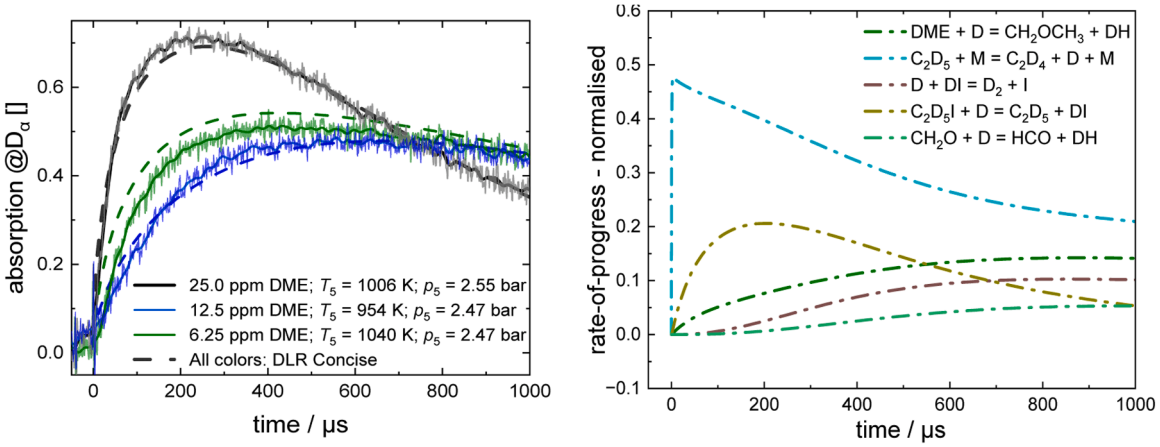

Fig. 4. Left: Measurements of mixtures of DME with C_2D_5I in argon at different concentrations at ratio of 5:1. Only D-ARAS profiles were measured for DME. Dashed curves: Simulations using the DLR Concise mechanism [29]. Right: ROP- analysis of D atoms for the experiment at 25 ppm and T_5 = 1006 K.

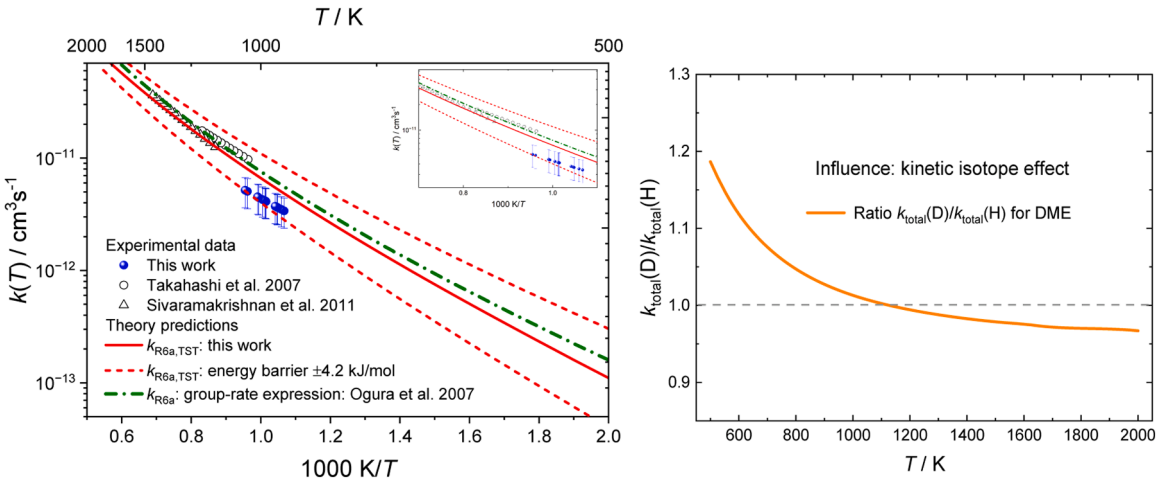

Fig. 5. Left: Comparison between measured (symbols) and theoretical predicted (curves) k_{R6a} values. Right: Ratio of $k_{R6a,TST}$ and $k_{R6b,TST}$ data for demonstrating that the kinetic-isotope effect can be safely neglected at $T > 900$ K.

bonds in ether compounds.

Computed energies of stationary points of the PES of reactions (R6a) and (R6b) are presented in Fig. 6. Please note that according to the ATcT [37], H_2 and HD should have very similar energies with differences below 1 kJ/mol at 0 K. The PES diagrams shown in this work indicate that HD is about 4.5 kJ/mol higher in energy than H_2. We want to point out that total electronic energies, as defined by the G4 compound model, including the zero-point energy, are identical for H and D, whereas the ATcT report different 0 K enthalpies of formation for H and D atoms. Considering that PES diagrams, such as the one in Fig. 6, show ZPE corrected electronic energies and not enthalpies, the issue related to energies of H and D atoms could be a reason for the apparent discrepancy related to the species HD.

5.4. H/D + DEE

In case of D/H + DEE ($CH_3CH_2OCH_2CH_3$), there are two possible H-atom abstraction channels:

$$D^\bullet + CH_3CH_2OCH_2CH_3 \leftrightharpoons HD + CH_3CH_2OCH_2CH_2^\bullet \quad \text{(R7a)}$$

$$D^\bullet + CH_3CH_2OCH_2CH_3 \leftrightharpoons HD + CH_3CH_2OCH^\bullet CH_3 \quad \text{(R8a)}$$

The analogue reactions considering H atoms as reaction partner of

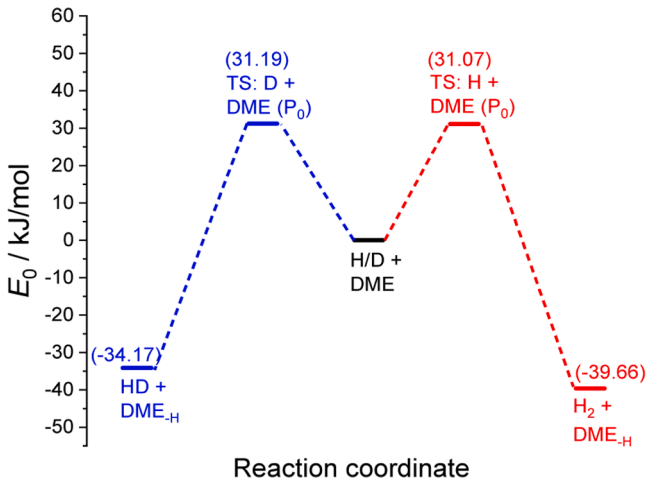

Fig. 6. PES (energies at $T = 0$ K including ZPE correction) of H-atom abstractions H/D + DME (R6a and R6b) obtained by applying the G4 composite method.

DEE are:

$$H^\bullet + CH_3CH_2OCH_2CH_3 \leftrightharpoons H_2 + CH_3CH_2OCH_2CH_2^\bullet \quad \text{(R7b)}$$

$$H^\bullet + CH_3CH_2OCH_2CH_3 \leftrightharpoons H_2 + CH_3CH_2OCH^\bullet CH_3 \quad \text{(R8b)}$$

(R7a) and (R7b) are H-atom abstraction from primary C–H bonds that have a slightly different chemical environment compared to DME. These six primary C–H bonds are categorized as P_1 (see Fig. 1). Besides P_1 bonds, there are four secondary bonds, which are designated as S_{0a}, indicating that these secondary bonds have one O atom in their neighborhood. Fig. 7 (left) shows D- and H-ARAS absorption profiles with modeling for an experiment at $T_5 = 977$ K and $p_5 = 2.42$ bar for an initial DEE mole fraction of 25 ppm (and 5 ppm C_2D_5I) diluted in argon. Modeling of absorption profiles was performed using an adjusted mechanism by Yasunaga *et al.* [5] – a detailed DEE reaction mechanism containing 751 reactions with 148 species involved based on extensive set of shock-tube experiments on DEE combustion. The right panel of Fig. 7 shows the D atom rate-of-progress analysis for that particular experiment based on the Yasunaga mechanism. It can be seen that H-atom abstraction reactions are energetically favored at the secondary position. Under the experimental conditions shown here, no competing reactions with D atoms were found.

For the experiment shown in Fig. 7 (left), a best fit simulation was obtained by adjusting the total H-atom abstraction rate coefficient of (R7a) and (R8a) from Yasunaga *et al.* each by a factor of 0.5. The fact that the modeling predicts a steeper increase in D atoms in the first 50 µs may be due to an uncertainty in the specific k_1 value (see Chapter 5.1). It is also possible that the H-atom abstraction reactions are expected to be too slow in these early reaction times. By applying this adjustment, the agreement between experiment and simulation is also enhanced for the H-ARAS profile. This also applies to measurements at higher temperatures up to 1235 K since in case of D + DEE, the release of H atoms is strongly linked to consecutive decomposition reactions of initially formed DEE radicals. The combination of D- and H-ARAS experiments indicates that modifying rate coefficients for initial H-atom abstractions has a significant impact on branching ratios of secondary reactions and hence, on the production of H atoms, which could also impact simulated ignition delay times.

The present D-ARAS experiments do not allow us to derive a branching ratio of the reactions (R7a) and (R8a). Only total H-atom abstraction rate coefficients, k_{D+DEE}, can be measured, with $k_{D+DEE} = k_{R7a} + k_{R8a}$. Experimentally determined reaction rate coefficients k_{D+DEE} and a comparison to theoretical predictions are shown in Fig. 8. Calculated energies of stationary points of the PES of reactions (R7a), (R7b), (R8a), and (R8b) are provided in Fig. 9.

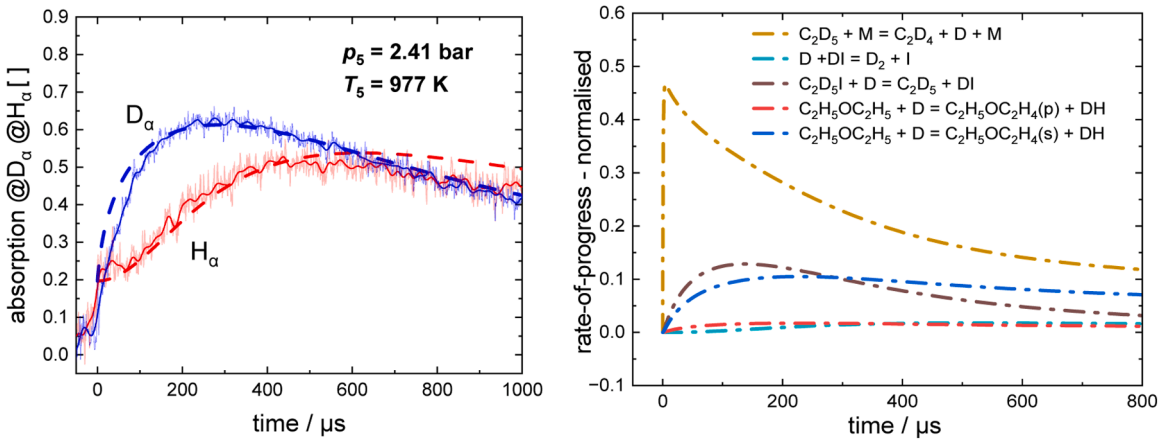

Fig. 7. Left: H- and D-ARAS absorption profiles for a mixture with 25 ppm DEE and 5 ppm C_2D_5I diluted in Ar. Dashed curves: Simulations based on an adjusted version of the Yasunaga *et al.* mechanism [5]. Right: ROP-analysis for the assessment of D-atom containing reactions using Yasunaga *et al.* mechanism [5] for same conditions as left.

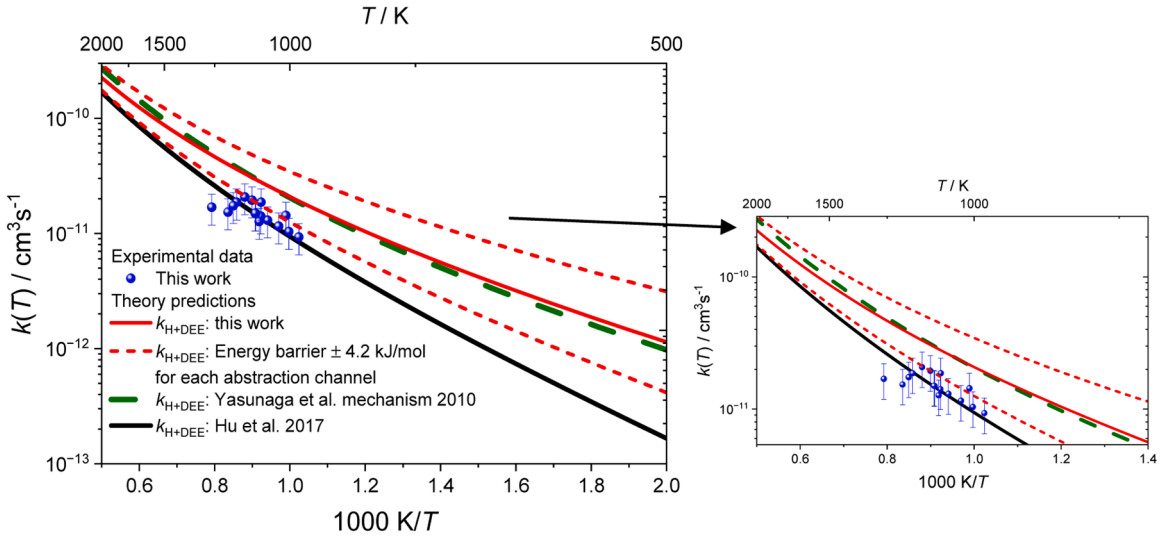

Fig. 8. Comparison between measured (symbols) and theoretical predicted (curves) k_{H+DEE} values. At $T = 900$ K, the kinetic isotope effect is below 5 %, *i.e.*, $k_{D+DEE}/k_{H+DEE} \leq 1.05$. Error bars represent an uncertainty of ±30 %. Dashed curves: Derived based on the assumption of an uncertainty of ±4.2 kJ/mol in energy barrier for each of the two H-atom abstraction channels.

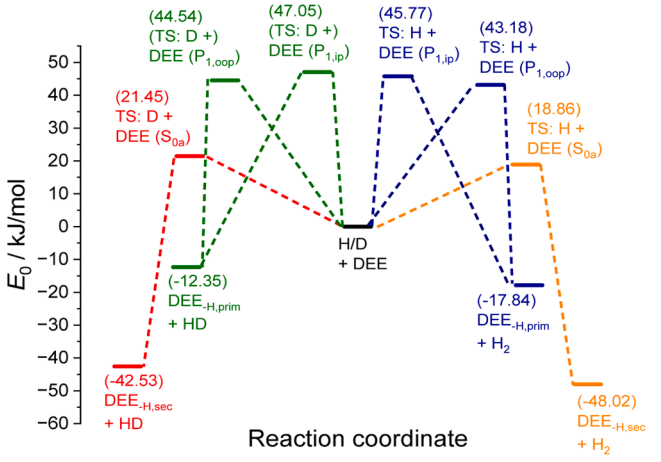

Fig. 9. PES (energies at 0 K including ZPE correction) of H-atom abstractions H/D + DEE (R7a-R8b) obtained by applying the G4 composite method.

Experimentally derived rate coefficients can be expressed for the temperature range 970–1270 K (at pressures between 2.1 – 2.5 bar) by the following Arrhenius equation:

$$k_{D+DEE,exp}(T) = 1.7\times10^{-10} \exp(-22.4 \text{ kJ/mol} / RT) \text{ cm}^3\text{s}^{-1} \quad (7)$$

The overall theoretical reaction rate coefficient for H + DEE ⇋ products is given by $k_{H+DEE} = 6k_{P1} + 4k_{S0a}$ because of the six primary bonds of type P_1 and the four secondary bonds of type S_{0a}. Since the kinetic isotope effect can be safely neglected at $T > 900$ K and due to a better visibility, in Fig. 8 and in the further figures that include comparisons between experimental and theory-based rate-coefficient data, only theory predictions for H-atom abstractions by H atoms will be given.

In analogy to DME, primary C–H bonds in DEE could also be differentiated between in-plane (ip) and out-of-plane (oop)bonds. According to the PES in Fig. 9, abstractions from ip and oop C–H bonds of P_1 type have slightly different energy barriers, i.e., 45.77 kJ/mol for ip-P_1 and 43.18 kJ/mol for oop-P_1. At $T < 700$ K, the slightly higher energy barrier for abstraction from ip-P_1 C–H bonds results in TST rate coefficients, which are ~ 10–25 % lower than those obtained for abstraction from oop-P_1 C–H bonds. Within the 700–1200 K

temperature range, the difference between theoretical rate coefficients for abstracting ip-P_1 and oop-P_1 C–H bonds is below 10 %. According to theory, ip and oop C–H P_1 bonds are different, but in such shock-tube experiments, the effects of having ip and oop bonds cannot be distinguished. To derive a theoretical expression for abstraction from C–H bonds of type P_1, the average between $k_{ip\text{-}P1}$ and $k_{oop\text{-}P1}$ (per C–H bond) was taken, *i.e.*, $k_{P1}(T) = (k_{ip\text{-}P1}(T) + k_{oop\text{-}P1}(T))/2$.

The present theory-based bond-type specific abstraction rate coefficients per C–H bond considering primary and secondary bonds are represented by the following equations:

$$k_{P1,DEE}(T) = 2.3\times10^{-18} \times T^{2.29} \exp(-33.7\ \text{kJ/mol} / RT)\ \text{cm}^3\text{s}^{-1} \quad (8)$$

$$k_{S0a,DEE}(T) = 1.2\times10^{-17} \times T^{2.07} \exp(-11.5\ \text{kJ/mol} / RT)\ \text{cm}^3\text{s}^{-1} \quad (9)$$

On average, the present TST results overpredict overall H-atom abstraction rate coefficients for H + DEE by a factor of two. Despite these deviations, measured and computed rate coefficients are still within the uncertainty ranges of experiment and theory. The TST prediction of this work is very close to the overall rate coefficient k_{H+DEE} given by the Arrhenius expression used in the Yasunaga *et al.* [5] reaction mechanism, *i.e.*, maximum deviations are within ±20 %. Hu *et al.* [55] conducted a theory and modeling study on DEE ignition. Among others, they reported *ab initio* TST based rate coefficient expressions for reactions (R7b) and (R8b). They carried out geometry optimizations and frequency analyses at the MP2/6-311-G(d,p) theory level and obtained energies of stationary points along the PES of DEE reactions applying the G3 composite method. Compared to our theoretical results and the modeling results from Yasunaga *et al.* [5], their TST-based rate coefficients are in agreement with the present experimental rate coefficients. Despite this very good agreement, it is certainly not possible to draw general conclusions regarding the overall performance of theory methods applied to study such H-atom abstractions.

As expected, H-atom abstraction from secondary C–H bonds is predicted to have lower energy barriers, which is also reflected in substantially larger rate coefficients of k_{S0a} compared to k_{P1}, *i.e.*, at 750 K $k_{P1,DEE} \approx 0.024\times k_{S0a,DEE}$, at 1000 K $k_{P1,DEE} \approx 0.062\times k_{S0a,DEE}$, and at 1250 K, $k_{P1,DEE} \approx 0.111\times k_{S0a,DEE}$. According to the TST results from Hu *et al.* [55], $k_{P1,DEE} \approx 0.033\times k_{S0a,DEE}$ at 750 K, $k_{P1,DEE} \approx 0.087\times k_{S0a,DEE}$ at 1000 K, and $k_{P1,DEE} \approx 0.155\times k_{S0a,DEE}$ at 1250 K.

5.5. H/D + DMM

Also, in case of H/D + DMM ($CH_3OCH_2OCH_3$), there are two possible H-atom abstraction channels:

$$D^\bullet + CH_3OCH_2OCH_3 \leftrightharpoons HD + CH_3OCH_2OCH_2^\bullet \quad (R9a)$$

$$D^\bullet + CH_3OCH_2OCH_3 \leftrightharpoons HD + CH_3OCH^\bullet OCH_3 \quad (R10a)$$

The analogue reactions considering H atoms as reaction partner of DMM are:

$$H^\bullet + CH_3OCH_2OCH_3 \leftrightharpoons H_2 + CH_3OCH_2OCH_2^\bullet \quad (R9b)$$

$$H^\bullet + CH_3OCH_2OCH_3 \leftrightharpoons H_2 + CH_3OCH^\bullet OCH_3 \quad (R10b)$$

(R9a) and (R9b) are H-atom abstraction from primary C–H bonds, which are expected to be analogue to primary C–H bonds in DME. Therefore, (R9a) and (R9b) represent abstractions from C–H bonds categorized as P_0. Since there is an O–CH_2–O moiety, one needs to consider a different type of secondary C–H bond, which is designated as S_{0b}. Therefore, following the group additivity rules, the overall rate coefficient for reactions H + DMM ⇌ products, k_{H+DMM}, is expected to be $k_{H+DMM} = 6k_{P0} + 2k_{S0b}$.

The presence of two methoxy moieties in DMM results in different conformers designated as gauche-gauche (gg), gauche-trans (gt), and trans-trans (tt). In previous quantum-chemical studies [56,57], the (gg) conformer was identified to be the most stable conformer. According to the G4 computations of the present work, the (gg) conformer is about 10.7 kJ/mol lower in energy compared to the two (gt) conformers and about 22.9 kJ/mol lower in energy compared to the (tt) conformer. Therefore, the (gg) conformer of DMM was considered for analyzing H/D + DMM reactions.

Fig. 10 (left) shows D- and H-atom absorption profiles simultaneously measured in this work compared to modeled profiles. Using the DLR Concise mechanism [29], adjusting total abstraction rate coefficients k_{D+DMM} and keeping the branching ratio for abstraction between (R9a) and (R10a) as reported by Kopp *et al.* [8], it was possible to obtain simulated best-fit D-atom absorption profiles (see Fig. 10, left) . However, simulated H-atom absorption profiles deviate significantly between measured profiles indicating uncertainties in consecutive reactions of initially formed DMM radicals. ROP-analysis (see Fig. 10, right) based on the described mechanism of reactions involving D atoms showed that H-atom abstraction reactions are most important for D-atom consumption. Under the experimental conditions shown, only reactions with formaldehyde (CH_2O) [52] and methyl (CH_3) contribute, but are significantly less effective. The reaction rate coefficient for CH_3 + D (+M) ⇌ CDH_3 (+M) was taken from Baulch *et al.* [58].

Fig. 11 shows rate coefficients k_{D+DMM} obtained from the present shock-tube experiments, k_{H+DMM} values reported by Golka *et al.* [12], and a comparison to TST predictions from this work and from Kopp *et al.* [8]. Fig. 12 shows the PES of H/D + DMM reactions obtained at the G4 level of theory.

Covering the 900 – 1300 K temperature range (at pressures between 2.1 – 2.4 bar), experimentally determined rate coefficients can be expressed by the Arrhenius equation given below:

$$k_{D+DMM,exp}(T) = 2.7\times10^{-10} \exp(-27.3\ \text{kJ/mol} / RT)\ \text{cm}^3\text{s}^{-1} \quad (10)$$

The present theory-based bond-type specific abstraction rate coefficients per C–H bond considering primary and secondary bonds, can then be represented by the following equations:

$$k_{P0,DMM}(T) = 2.4\times10^{-18} \times T^{2.23} \exp(-20.8\ \text{kJ/mol} / RT)\ \text{cm}^3\text{s}^{-1} \quad (11)$$

$$k_{S0b,DMM}(T) = 3.5\times10^{-18} \times T^{2.25} \exp(-21.2\ \text{kJ/mol} / RT)\ \text{cm}^3\text{s}^{-1} \quad (12)$$

Note that $k(T)$ values for abstraction from P_0 C–H bond types have been also computed for H + DMM. It is intended to test to which extent abstraction rate coefficients for analogue bond types in different ether compounds are similar to each other. Comparing k_{P0} expressions of DMM (Eq. 11) and DME (Eq. 5) indicates that above 800 K, $k_{P0,DME}(T) \approx 1.1\times k_{P0,DMM}(T)$. At least for DME and DMM, analogue C–H bond types seem to be of very similar reactivity. At least, such small reactivity differences can certainly not be probed by common high-temperature gas-phase kinetics experiments.

According to G4 computations, there seems to be no substantial difference in energy barriers for abstraction from S_{0b} sites and P_0 sites, however, according to the G4-based TST computations, in the range from 800 to 1200 K, $k_{P0}(T) \approx 0.61\times k_{S0b}(T)$. The reactivity difference towards H-atom abstraction between P_1 and S_{0b} C–H sites seems to be much less pronounced compared to P_0 and S_{0a} sites. Even though there appear to be differences in activation energies, the present ab initio TST prediction agrees well with the rate-coefficient datasets from this work and from Golka *et al.* [12], which also performed shock-tube experiments with ARAS diagnostic at the Lyman-α wavelength. The apparently low experimentally based activation energies could be related to the limited temperature range of the shock-tube experiments. In the present D-ARAS experiments, the limitation is related to the issue that the D-atom precursor decays quite slowly at temperatures below 950 K, while the thermal decomposition of the ether compounds starts to have a larger influence at temperatures above 1200-1300 K. Rate-coefficient values measured at the upper or lower limit of the temperature range show a greater uncertainty and can in turn result in larger uncertainties in the activation energies. We assume that this problem could also apply

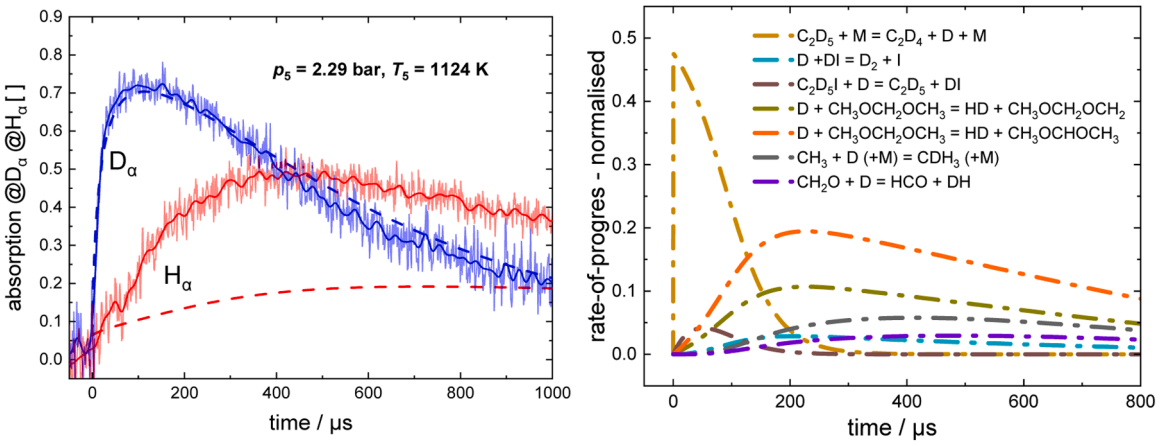

Fig. 10. Left: H- and D-ARAS profiles resulting from an experiment with 12.5 ppm DMM and 2.5 ppm C_2D_5I. Dashed curves show the modeled absorption profiles based on the DLR Concise mechanism [29]. Right: Corresponding ROP analysis, based on DLR Concise mechanism, showing H-atom abstraction reactions and further reactions involving D atoms.

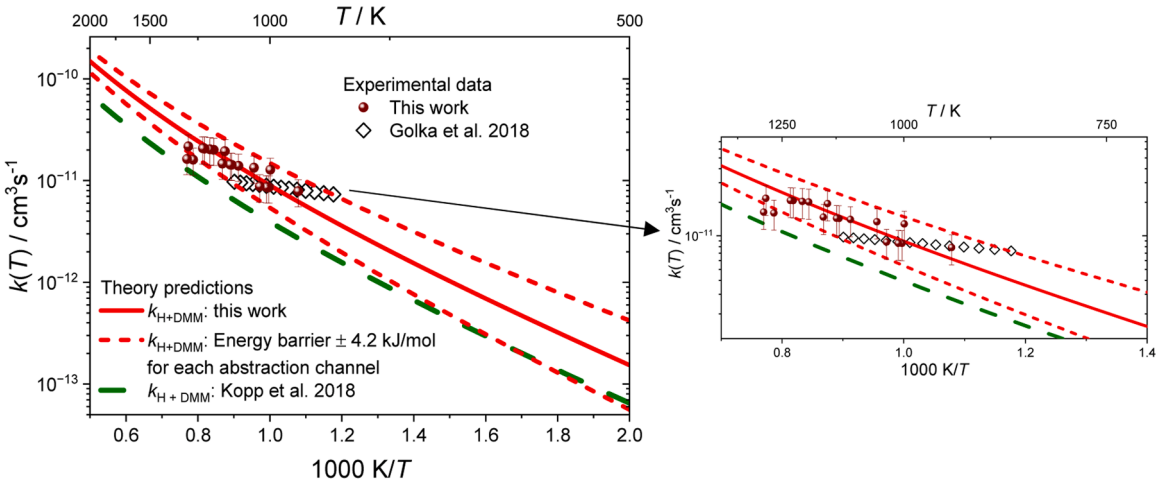

Fig. 11. Comparison between measured (symbols) and theoretical predicted (curves) for k_{H+DMM} values. Error bars represent an uncertainty of ±30 %. Dashed curves: Derived based on the assumption of an uncertainty of ± 4.2 kJ/mol in energy barrier for each of the two H-atom abstraction channels.

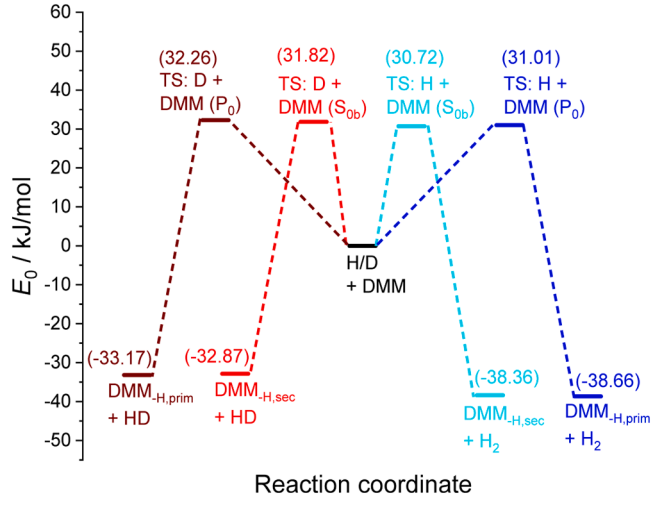

Fig. 12. PES (energies at 0 K including ZPE correction) of H-atom abstractions H/D + DMM (R9a-R10b) obtained by applying the G4 composite method.

for the experimental data from Golka *et al.* [12]. Besides the present TST prediction, Kopp *et al.* [8] conducted a high-level theory study on reaction H + DMM → products + H_2 at the CCSD(T)/aug-cc-pV(D+T)Z//B2PLYPD3BJ/6-311++g(d,p) level of theory. Over the whole 500–2000 K temperature range, the predicted k_{H+DMM} values from Kopp *et al.* [8] are approximately two times lower compared to the present theoretical values. The difference is related to deviations between rate coefficients for abstraction from primary C–H bonds, *i.e.*, $k_{P1}(T)$ values from Kopp *et al.* are around five times lower than the present $k_{P1}(T)$ values, whereas predictions for abstraction from secondary C–H bonds are in very good agreement, *i.e.*, theoretical predictions for $k_{S0b}(T)$ from Kopp *et al.* and from this work deviate by not more than approximately 12 %.

5.6. H/D + MPE

Methyl propyl ether (MPE) – its structure shown in Fig. 1 – contains four different C–H-bonds; therefore, being the most complex molecule examined in this work. For D + MPE, the following bimolecular reaction channels can occur:

$$D^\bullet + CH_3OCH_2CH_2CH_3 \rightleftharpoons HD + {}^\bullet CH_2OCH_2CH_2CH_3 \quad \text{(R11a)}$$

$$D^\bullet + CH_3OCH_2CH_2CH_3 \rightleftharpoons HD + CH_3OCH_2CH_2CH_2^\bullet \quad \text{(R12a)}$$

$D^{\bullet} + CH_3OCH_2CH_2CH_3 \leftrightharpoons HD + CH_3OCH_2CH^{\bullet}CH_3$ (R13a)

$D^{\bullet} + CH_3OCH_2CH_2CH_3 \leftrightharpoons HD + CH_3OCH^{\bullet}CH_2CH_3$ (R14a)

The analogue reactions considering H atoms as reaction partner of MPE are:

$H^{\bullet} + CH_3OCH_2CH_2CH_3 \leftrightharpoons H_2 + {}^{\bullet}CH_2OCH_2CH_2CH_3$ (R11b)

$H^{\bullet} + CH_3OCH_2CH_2CH_3 \leftrightharpoons H_2 + CH_3OCH_2CH_2CH_2^{\bullet}$ (R12b)

$H^{\bullet} + CH_3OCH_2CH_2CH_3 \leftrightharpoons H_2 + CH_3OCH_2CH^{\bullet}CH_3$ (R13b)

$H^{\bullet} + CH_3OCH_2CH_2CH_3 \leftrightharpoons H_2 + CH_3OCH^{\bullet}CH_2CH_3$ (R14b)

In detail, (R11a) and (R11b) represent abstractions from P_0 C–H sites (analogue to DMM and DME), (R12a) and (R12b) represent abstractions from P_1 sites (analogue to DEE), (R13a) and (R13b) represent abstractions from secondary C–H bonds categorized as S_1 (see Fig. 1), and (R14a) and (R14b) represent abstractions from S_{0a} sites (analogue to DEE). Hence, the overall reaction rate coefficient of (R11b to (R14b) – k_{H+MPE} – is expected to be $3k_{P0} + 3k_{P1} + 2k_{S1} + 2k_{S0a}$. Similar to DMM, there is an OCH_3 moiety in MPE resulting in the possibility of trans-trans (tt) and trans-gauche (tg) conformers. According to the G4 computations of the present work, the (tg) conformer is computed to be about only 0.6 kJ/mol lower in energy compared to the (tt) conformer. This is such a small energy difference that, based on the G4 computations, one cannot clearly state, which of the two conformers is of lower energy. However, since the G4 method predicts the (tg) conformer to be of slightly lower energy, *ab initio* TST computations have been conducted on that conformer.

Chemical-kinetics studies related to MPE are sparse. To the best of our knowledge, the most comprehensive reaction mechanism was published by Johnson *et al.* in 2021 [44]. This model was constructed using the Reaction Mechanism Generator (RMG) [59]. Refinement of the model for stoichiometric combustion was conducted at 400-1650 K and 0.3-100 bar, thereby showing an overlap with conditions measured in this work. Fig. 13 shows simultaneously measured D- and H-atom absorption profiles obtained during a shock-tube experiment at $T_5 = 1214$ K and $p_5 = 2.44$ bar. Note that the Arrhenius expression of the competitive recombination reaction $D + CH_3$ (+M) ⇌ CH_3D (+M) is also achieved by applying the RMG approach, like all reactions included in this model.

By minor adjusting the overall rate coefficient of (R11a) to (R14ba) – k_{D+MPE} – and keeping the branching ratio between the different H-atom abstraction channels as given in the reaction mechanism from ref. [44], it was possible to obtain best-fit D-atom absorption profiles. Following the adjustment of k_{D+MPE}, simulated H-atom absorption profiles also nicely fit to the measured ones (see Fig. 13, red symbols and red curves); this finding suggests that this reaction mechanism not only succeeds in describing the kinetics of H-atom abstraction reactions but also of secondary reactions of initially formed MPE radicals.

Experimentally determined reaction rate coefficients – $k_{exp,total\ (D+MPE)}$ – and comparison to predictions from the Johnson *et al.* [44] mechanism and from present *ab initio* TST computations are shown in Fig. 14; Fig. 15 shows the potential energy surface (PES) of the respective H/D + MPE reactions obtained at the G4 level of theory.

Over the 1000–1350 K temperature range (at pressures between 2.1 and 2.7 bar), the experimentally derived rate coefficients $k_{(D+MPE)exp}$ can be represented by the following Arrhenius equation:

$$k_{(D+MPE),exp}(T) = 5.1\times10^{-10} \exp(-31.5\ \text{kJ/mol} / RT)\ \text{cm}^3\text{s}^{-1} \quad (13)$$

The present theory-based bond-type specific abstraction rate coefficients per C–H bond are represented by the following equations:

$$k_{P0,MPE}(T) = 2.8\times10^{-19} \times T^{2.51} \exp(-15.9\ \text{kJ/mol} / RT)\ \text{cm}^3\text{s}^{-1} \quad (14)$$

$$k_{P1,MPE}(T) = 2.2\times10^{-19} \times T^{2.54} \exp(-26.5\ \text{kJ/mol} / RT)\ \text{cm}^3\text{s}^{-1} \quad (15)$$

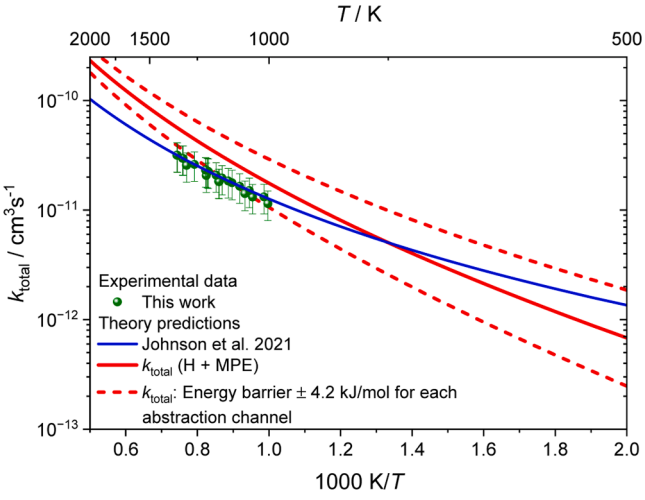

Fig. 14. Comparison between measured (symbols) and theoretical predicted (red curve) k_{D+MPE} values. Error bars represent an uncertainty of ±30 %. Dashed curves: Derived based on the assumption of an uncertainty of ±4.2 kJ/mol in energy barrier for each of the four H-atom abstraction channels. Blue solid curve: k_{D+MPE} according to unmodified Johnson *et al.* [44].

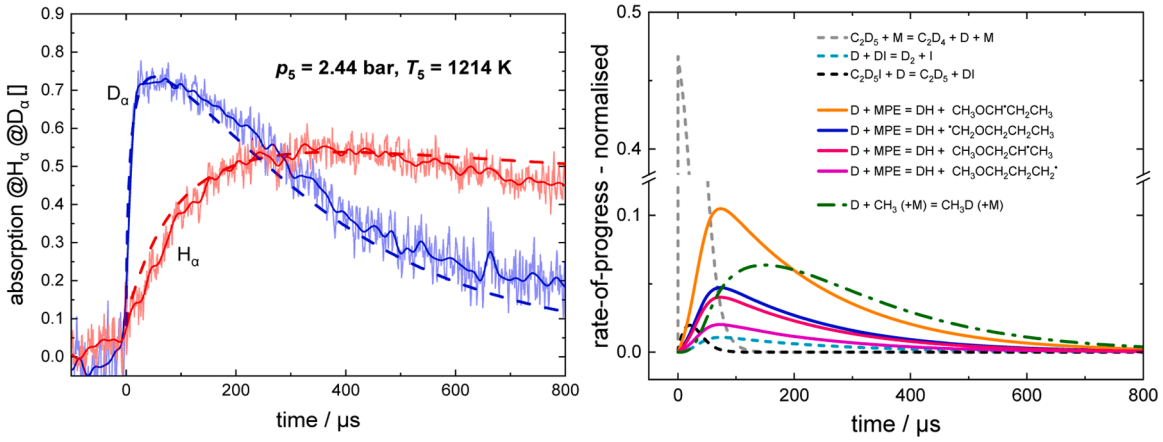

Fig. 13. Left: Absorption measurements of a mixture with 12.50 ppm MPE and 2.50 ppm C_2D_5I, diluted in argon. Dashed curves: Simulated absorption profiles based on the Johnson *et al.* [44] mechanism extended by C_2D_5I-decay and D atom consuming reactions [44]. Right: ROP-analysis using the same mechanism showing those reactions contributing the most to D-atom consumption.

$$k_{S1,MPE}(T) = 4.0\times10^{-18} \times T^{2.2} \exp(-23.1\ \text{kJ/mol} / RT)\text{cm}^3\text{s}^{-1} \quad (16)$$

$$k_{S0a,MPE}(T) = 1.1\times10^{-17} \times T^{2.08} \exp(-11.9\ \text{kJ/mol} / RT)\ \text{cm}^3\text{s}^{-1} \quad (17)$$

Different energy barriers of H-atom abstraction channels (see Fig. 15) result in different reactivities towards H-atom abstraction; in detail, at $T = 1000$ K, $k_{P1,MPE} < k_{P0,MPE} \approx k_{S1,MPE} < k_{S0a,MPE}$. C–H bond types S_{0a}, S_1, and P_0 also appear in other investigated ether compounds (see Fig. 1). As mentioned above, repeating *ab initio* TST computations for analogue bond types were carried out to test to which extent similar bond types in different ether compounds are similar to each other. A more detailed comparison of analogue bond types in various ether compounds will be given in the following section (discussion). Across the 500–2000 K temperature range, deviations between $k_{S0a,MPE}(T)$ and $k_{S0a,DEE}(T)$ are way below 10 %; therefore, S_{0a} sites in different ethers seem to have almost identical reactivity towards H-atom abstraction. However, P_0 bonds in MPE result in $k_{P0}(T)$ values which deviate by more than 40 % compared to $k_{P0}(T)$ values of DME and DMM at temperatures below 1000 K.

Present *ab initio* TST predictions and experimental k_{D+MPE} data are well within their uncertainties. There is a remarkably good agreement between the RMG generated prediction for k_{H+MPE} given in the reaction mechanism from Johnson *et al.* [44] and the present experimentally determined reaction rate coefficient values. Considering the deviations in TST prediction of the present work and those of RMG-generated k_{H+MPE} data, we checked if there is also a significant difference regarding the simulated branching ratios. Predicted branching ratios are shown in Fig. 16.

Even though absolute rate-coefficient values and the overall temperature dependence of k_{H+DMM} are different, the predictions of this work and those of Johnson *et al.* [44] result in similar values of the specific branching ratios. Due to the complexity of an RMG generated reaction mechanism, it is difficult to assess the reason for this observed deviation between predicted overall k_{H+MPE} data.

6. Discussion

Here, a more detailed comparison of analogue bond types in the four oxygenated molecules will be given. First, we are focusing on the comparison between computed abstraction rate coefficients per bond-type specific C–H bonds. Fig. 17 summarizes G4-based TST predictions of H-atom abstraction rate coefficients per C–H bond for the four ethers considered. Since theory determined and experimentally derived rate-coefficient data agree quite well, as shown previously in Figs. 5,8,11,14, the TST results are expected to predict overall reactivity trends towards H-atom abstraction by H atoms.

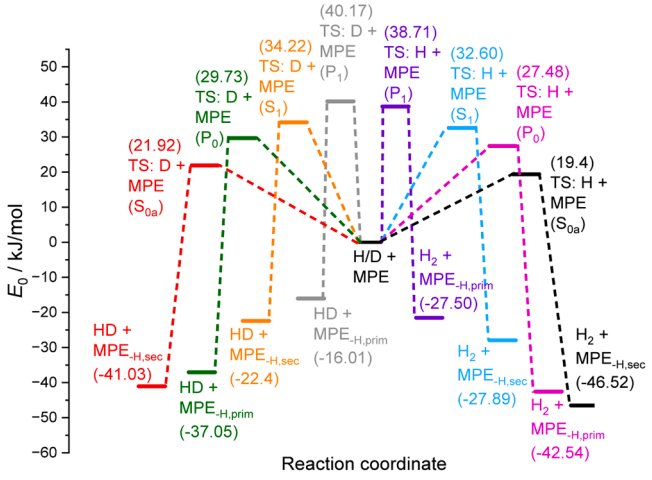

Fig. 15. PES (energies at 0 K including ZPE correction) of H-atom abstractions H/D + MPE (R11a-R14b) obtained by applying the G4 composite method.

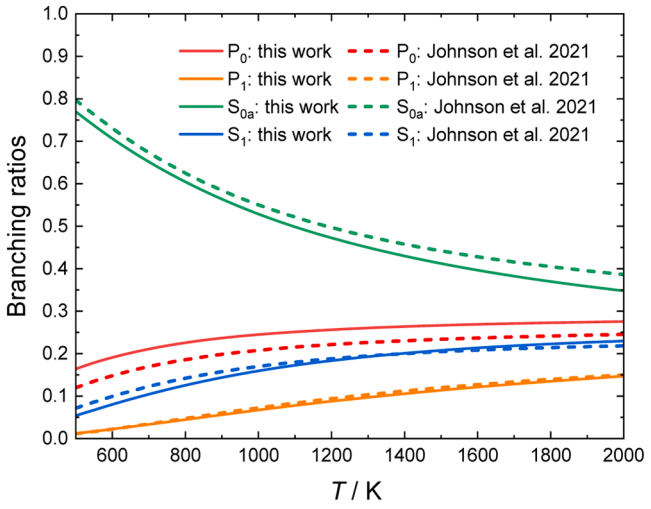

Fig. 16. Predicted branching ratios of different H-atom abstraction channels from overall reaction H + MPE → products + H_2. Branching ratios (BR) are given by: $BR_{P0} = 3k_{P0}/k_{total}$, $BR_{P1} = 3k_{P1}/k_{total}$, $BR_{S1} = 2k_{S1}/k_{total}$, and $BR_{S0a} = 2k_{S0a}/k_{total}$, with $k_{total} = 3k_{P0} + 3k_{P1} + 2k_{S1} + 2k_{S0a}$.

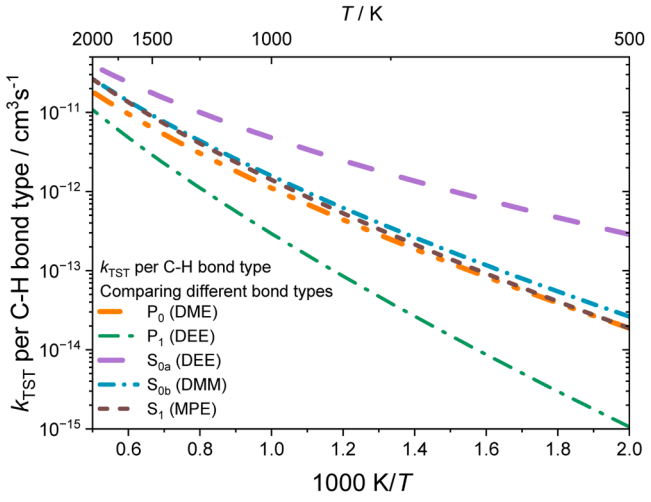

Fig. 17. Comparison between computed abstraction rate coefficients per bond-type specific C–H bonds using TST. P_0, P_1, S_{0a}, S_{0b} and S_1 categorize C–H bond types as described previously. Each C–H bond is taken from one of the investigated linear ethers from this work.

Depending on the type of C-H bond, considerable differences can be observed in the computed $k(T)$ data. The energy barriers for H-atom abstraction from different C-H bond types are not that pronounced, but the related partition functions, especially the vibrational partition function, can show different temperature dependencies. In larger ether molecules, in which there are a larger number of C-H bonds and an overall larger number of different C-H bond types, these small differences will add up and could then finally result in significant deviations. According to Fig. 17, P_1 C–H bonds are suggested to have the lowest reactivity towards H-atom abstraction (green, dash-dotted curve), whereas S_{0a} C–H bonds are found to have the highest reactivity among the considered C–H bond types (pink, dashed curve). P_0, S_1, and S_{0b} bonds are identified to have quite similar reactivities, which are indicated to be between those of P_1 and S_{0a}. Among P_0, S_1, and S_{0b}, we have observed, on average over the whole temperature range, the order $k_{P0} < k_{S1} < k_{S0b}$, although the differences are quite small, *i.e.*, not more than a factor of two.

Since secondary C–H bonds have lower bond-dissociation energies than primary bonds, it is clear that abstraction from S_1-type bonds is preferred compared to abstraction from P_1-type bonds. The difference between P_1 and P_0 can be also well understood, since abstraction from a P_0-type C–H bond results in the formation of a primary resonance-stabilized radical. Forming a primary resonance-stabilized radical is suggested to have a similar effect like abstraction from a secondary C–H bond (S_1 type), which leads to the formation of a secondary radical without additional resonance stabilization. The substantially higher expected reactivity of S_{0a} type C–H bonds compared to P_1, S_1, and P_0 bonds is also well understandable, since abstraction from S_{0a}-type C–H bonds results in the formation of secondary resonance-stabilized radicals. The difference between S_{0a} and S_{0b} is maybe not that obvious. H-atom abstraction from a S_{0b} C–H bond as in DMM is predicted to be of much lower reactivity compared to abstraction from S_{0a}-type C–H bonds. Abstraction from S_{0b} C–H bonds yields secondary radicals, for which three resonant structures can be formulated (R–O–CH$^\bullet$–O–R ↔ R-O$^\bullet$=CH–O–R ↔ R–O–CH=O$^\bullet$-R); however, this stabilizing effect seems to be overcompensated by the negative inductive effect of the two neighboring O atoms which has a destabilizing impact on that secondary radical.

Also, it is interesting to analyze the results of the Arrhenius expressions for H-atom abstraction depending on the specific C–H bond types of the four ethers investigated in the present study. Fig. 18 compares TST computed rate-coefficient data for abstraction of analogue C–H bond types occurring in different ether compounds.

According to Fig. 18, analogue P_0 and P_1 C–H bond types occurring in different compounds reveal significant differences. At temperatures below 1000 K, $k_{P1,MPE}$ and $k_{P1,DEE}$ deviate from each other and with respect to bond type P_0, $k_{P0,MPE}$ is deviating from $k_{P0,DME}$ and $k_{P0,DMM}$ indicating that establishing quantitatively accurate rate-rule expressions for a well-known reaction class such as H-atom abstractions is still not that straight-forward. However, Fig. 18 also clearly shows that different bond types lead to distinguishable reactivities; these reactivity trends are overall in good agreement with the experimental results obtained in this work.

To provide an approximative expression of $k_{P0}(T)$ and $k_{P1}(T)$ for H-atom abstraction by H atoms, we take the arithmetic averages of $k_{P0,DME}$, $k_{P0,DMM}$, and $k_{P0,MPE}$ as well as $k_{P1,DEE}$ and $k_{P1,MPE}$, *i.e.*, $k_{P0} = (k_{P0,DME} + k_{P0,DMM} + k_{P0,MPE})/3$ and $k_{P1} = (k_{P1,DEE} + k_{P1,MPE})/2$:

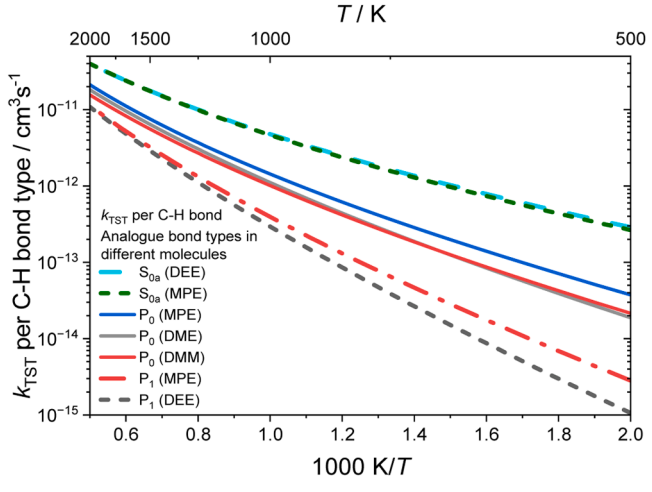

Fig. 18. Comparison among TST computed bond-type specific abstraction rate coefficients. Here, TST predictions of H-atom abstractions of analogue bond types appearing in different ether compounds are compared. P_0, P_1, S_{0a}, S_{0b} and S_1 categorize C–H bond types as described previously. Dashed curves represent reaction rate coefficients in S_{0a} C–H bonds, solid curves in P_0 and dotted curves in S_{0a} C–H bonds.

$$k_{P0}(T) \approx 7.1\times10^{-19} \times T^{2.39} \exp(-18.2\ \text{kJ/mol} / RT)\ \text{cm}^3\text{s}^{-1} \quad (18)$$

$$k_{P1}(T) \approx 2.6\times10^{-19} \times T^{2.54} \exp(-28.6\ \text{kJ/mol} / RT)\ \text{cm}^3\text{s}^{-1} \quad (19)$$

To also obtain an approximative expression for $k_{S0a}(T)$, we also take the average, *i.e.*, $k_{S0a} = (k_{S0a,DEE} + k_{S0a,MPE})/2$:

$$k_{S0a}(T) \approx 1.1\times10^{-17} \times T^{2.08} \exp(-11.7\ \text{kJ/mol} / RT)\ \text{cm}^3\text{s}^{-1} \quad (20)$$

C–H bond types designated as S_1 and S_{0b} only appear once in the ether compounds considered, *i.e.*, S_1 in MPE and S_{0b} in DMM. So far, only the approximation $k_{S0b}(T) \approx k_{S0b,DMM}(T)$ and $k_{S1}(T) \approx k_{S1,MPE}(T)$ is possible.

7. Conclusions

To the best of our knowledge, this present study represents the most comprehensive effort to date using the sensitive D-ARAS technique to determine reaction rate coefficients of different H + ether H-atom abstraction reactions. We have also developed bond-type specific rate-coefficient expressions based on a combination of TST calculations and experimental data.

Using D-ARAS shock-tube experiments, total rate coefficients of H-atom abstractions of four oxygenated ethers – in detail dimethyl ether (DME), diethyl ether (DEE), dimethoxymethane (DMM) and methyl propyl ether – were determined at elevated pressures for temperatures of 927–1346 K. Deuterated ethyl iodide C_2D_5I was used as a D-atom precursor allowing the differentiation between H-atom abstraction reactions (connected to consumption of D atoms) and – in the later course of reaction – the increase in $[H]_t$ caused by ether decomposition.

The four ether compounds examined contain a total of five different C–H bond types. Two primary bonds classified as P_0 and P_1, and three secondary bonds classified as S_{0a}, S_{0b}, and S_1. For each type of bond, rate coefficients for H-atom abstraction have been computed using TST based on *ab initio* properties obtained at the G4 level of theory. Based on the concept of additivity of bond-type specific rate coefficients – designated as k_{P0}, k_{P1}, k_{S1}, k_{S0a}, and k_{S0b} per C–H bond – total H-atom abstraction rate coefficients of each reaction studied were obtained by summing up the respective bond-specific rate coefficients. The total abstraction reaction rate coefficients based on TST were found to be in very good agreement, with the experimentally determined rate coefficients, with a difference of only ±20–45 %.

By combining elementary-kinetics experiments and TST computations, we were able to estimate bond-type specific rate-coefficient expressions for H-atom abstraction reactions. We have made substantial efforts to establish rate-rule expressions for reactions between H radicals and various groups of hydrocarbons.

Novelty and significance statement

The newly established experimental setup of a shock tube presented here in combination with two simultaneously operated H- and D-ARAS detection lines enabled the comparison of structurally varying linear ethers. A notable advantage of this approach was the use of a deuterated precursor, C_2D_5I, which allowed the distinction between H-atom abstraction and ether decay. To our knowledge, this approach has not yet been performed on linear ethers with a focus on this class of reactions and, for example, made it possible to test a detailed reaction mechanism for methyl propyl ether combustion, which was generated by the reaction mechanism generator (RMG) software.

The experiments were complemented by a theory analysis. By means of transition-state theory (TST) computations, C–H bond type specific $k(T)$ expressions were derived; by combining such bond-type related $k(T)$ data, overall H-atom abstraction rate coefficient data were obtained, which were then compared with experimental $k(T)$ values. The combination of this methodology with direct measurements of high-temperature rate coefficient data is a unique point of the present work and enables a detailed comparison of H-atom abstractions in linear ethers depending on different C–H bond types.

CRediT authorship contribution statement

F. Werner: Methodology, Visualization, Writing – review & editing. **C. Naumann:** Resources, Supervision, Writing – review & editing, Funding acquisition. **M. Braun-Unkhoff:** Writing – review & editing, Supervision, Funding acquisition. **T. Methling:** Validation, Writing – review & editing. **C. Schulz:** Project administration, Conceptualization, Funding acquisition, Writing – review & editing. **U. Riedel:** Project administration, Conceptualization, Funding acquisition, Writing – review & editing. **S. Peukert:** Project administration, Conceptualization, Funding acquisition, Visualization, Writing – review & editing.

Declaration of competing interest

The authors declare that they have no known competing financial interests or personal relationships that could have appeared to influence the work reported in this paper.

Acknowledgement

We acknowledge financial support by the German Research Foundation (DFG project "Structure-reactivity relationships and reaction mechanisms for future fuel components"; project number 427458221).

Supplementary materials

Supplementary material associated with this article can be found, in the online version, at doi:10.1016/j.combustflame.2024.113689.

References

[1] A.L. Boehman, Dimethyl ether special section, Fuel Process. Technol. 89 (2008) 1243–1478.
[2] R. Sivaramakrishnan, J.V. Michael, A.F. Wagner, R. Dawes, A.W. Jasper, L. B. Harding, Y. Georgievskii, S.J. Klippenstein, Roaming radicals in the thermal decomposition of dimethyl ether: experiment and theory, Combust. Flame 158 (2011) 618–632.
[3] Z. Wang, X. Zhang, L. Xing, L. Zhang, F. Herrmann, K. Moshammer, F. Qi, K. Kohse-Höinghaus, Experimental and kinetic modeling study of the low- and intermediate-temperature oxidation of dimethyl ether, Combust. Flame 162 (2015) 1113–1125.
[4] U. Burke, K.P. Somers, P. O'Toole, C.M. Zinner, N. Marquet, G. Bourque, E. L. Petersen, W.K. Metcalfe, Z. Serinyel, H.J. Curran, An ignition delay and kinetic modeling study of methane, dimethyl ether, and their mixtures at high pressures, Combust. Flame 162 (2015) 315–330.
[5] K. Yasunaga, F. Gillespie, J.M. Simmie, H.J. Curran, Y. Kuraguchi, H. Hoshikawa, M. Yamane, Y. Hidaka, A multiple shock tube and chemical kinetic modeling study of diethyl ether pyrolysis and oxidation, J. Phys. Chem. A 114 (2010) 9098–9109.
[6] J. Burger, M. Siegert, E. Ströfer, H. Hasse, Poly(oxymethylene) dimethyl ethers as components of tailored diesel fuel: Properties, synthesis and purification concepts, Fuel 89 (2010) 3315–3319.
[7] J. Burger, E. Ströfer, H. Hasse, Production process for diesel fuel components poly (oxymethylene) dimethyl ethers from methane-based products by hierarchical optimization with varying model depth, Chem. Eng. Res. Des. 91 (2013) 2648–2662.
[8] W.A. Kopp, L.C. Kröger, M. Döntgen, S. Jacobs, U. Burke, H.J. Curran, K.A. Heufer, K. Leonhard, Detailed kinetic modeling of dimethoxymethane. part I: Ab initio thermochemistry and kinetics predictions for key reactions, Combust. Flame 189 (2018) 433–442.
[9] L. Marrodán, E. Royo, Á. Millera, R. Bilbao, M.U. Alzueta, High pressure oxidation of dimethoxymethane, Energy & Fuels 29 (2015) 3507–3517.
[10] F.H. Vermeire, H.-H. Carstensen, O. Herbinet, F. Battin-Leclerc, G.B. Marin, K. M. Van Geem, Experimental and modeling study of the pyrolysis and combustion of dimethoxymethane, Combust. Flame 190 (2018) 270–283.
[11] S. Peukert, P. Sela, D. Nativel, J. Herzler, M. Fikri, C. Schulz, Direct measurement of high-temperature rate constants of the thermal decomposition of dimethoxymethane, a shock tube and modeling study, J. Phys. Chem. A 122 (2018) 7559–7571.
[12] L. Golka, I. Weber, M. Olzmann, Pyrolysis of dimethoxymethane and the reaction of dimethoxymethane with H atoms: A shock-tube/ARAS/TOF-MS and modeling study, Proc. Combust. Inst. 37 (2019) 179–187.
[13] L. Golka, D. Gratzfeld, I. Weber, M. Olzmann, Temperature- and pressure-dependent kinetics of the competing C–O bond fission reactions of dimethoxymethane, Phys. Chem. Chem. Phys. 22 (2020) 5523–5530.
[14] T.M. Pazdera, J. Wenz, M. Olzmann, The unimolecular decomposition of dimethoxymethane: channel switching as a function of temperature and pressure, Faraday Discuss 238 (2022) 665–681.
[15] T. Yu, X. Wu, X. Zhou, A. Bodi, P. Hemberger, Hydrogen migration as a potential driving force in the thermal decomposition of dimethoxymethane: New insights from pyrolysis imaging photoelectron photoion coincidence spectroscopy and computations, Combust. Flame 222 (2020) 123–132.
[16] M. Döntgen, M.E. Fuller, S. Peukert, D. Nativel, C. Schulz, K.A. Heufer, C. F. Goldsmith, Shock tube study of the pyrolysis kinetics of Di- and trimethoxy methane, Combust. Flame 242 (2022) 112186.
[17] R.D. Cook, D.F. Davidson, R.K. Hanson, Shock tube measurements of ignition delay times and OH time-histories in dimethyl ether oxidation, Proc. Combust. Inst. 32 (2009) 189–196.
[18] J.F. Bott, N. Cohen, A shock tube study of the reaction of the hydroxyl radical with propane, Int. J. Chem. Kinet. 16 (1984) 1557–1566.
[19] J.F. Bott, N. Cohen, A shock tube study of the reaction of the hydroxyl radical with H_2, CH_4, c-C_5H_{10}, and i-C_4H_{10}, Int. J. Chem. Kinet. 21 (1989) 485–498.
[20] J.F. Bott, N. Cohen, A shock tube study of the reactions of the hydroxyl radical with several combustion species, Int. J. Chem. Kinet. 23 (1991) 1075–1094.
[21] R. Sivaramakrishnan, N.K. Srinivasan, M.C. Su, J.V. Michael, High temperature rate constants for OH+ alkanes, Proc. Combust. Inst. 32 (2009) 107–114.
[22] R. Sivaramakrishnan, J.V. Michael, Rate constants for oh with selected large alkanes: shock-tube measurements and an improved group scheme, J. Phys. Chem. A 113 (2009) 5047–5060.
[23] H.-H. Carstensen, A.M. Dean, Rate constant rules for the automated generation of gas-phase reaction mechanisms, J. Phys. Chem. A 113 (2009) 367–380.
[24] R. Sivaramakrishnan, J.V. Michael, B. Ruscic, High-temperature rate constants for H/D + C_2H_6 and C_3H_8, Int. J. Chem. Kinet. 44 (2012) 194–205.
[25] S.L. Peukert, R. Sivaramakrishnan, J.V. Michael, High temperature rate constants for H/D+n-C_4H_{10} and i-C_4H_{10}, Proc. Combust. Inst. 35 (2015) 171–179.
[26] T. Ogura, A. Miyoshi, M. Koshi, Rate coefficients of H-atom abstraction from ethers and isomerization of alkoxyalkylperoxy radicals, Phys. Chem. Chem. Phys. 9 (2007) 5133–5142.
[27] S.L. Peukert, R. Sivaramakrishnan, J.V. Michael, High temperature shock tube and theoretical studies on the thermal decomposition of dimethyl carbonate and its bimolecular reactions with H and D-atoms, J. Phys. Chem. A 117 (2013) 3718–3728.
[28] S.L. Peukert, J.V. Michael, High-temperature shock tube and modeling studies on the reactions of methanol with D-atoms and CH_3-radicals, J. Phys. Chem. A 117 (2013) 10186–10195.
[29] T. Kathrotia, P. Oßwald, C. Naumann, S. Richter, M. Köhler, Combustion kinetics of alternative jet fuels, Part-II: Reaction model for fuel surrogate, Fuel 302 (2021) 120736. https://dlr.de/vt/mechanisms (accessed 122022/120711/120711).
[30] S. Peukert, C. Naumann, M. Braun-Unkhoff, U. Riedel, Formation of H-atoms in the pyrolysis of cyclohexane and 1-hexene: A shock tube and modeling study, Int. J. Chem. Kinet. 43 (2011) 107–119.
[31] P. Glarborg, J.A. Miller, B. Ruscic, S.J. Klippenstein, Modeling nitrogen chemistry in combustion, Prog. Energy Combust. Sci. 67 (2018) 31–68.
[32] K.M. Pamidimukkala, G.B. Skinner, Resonance absorption measurements of atom concentrations in reacting gas mixtures. VIII. Rate constants for O+H_2→OH+H and O+D_2→OD+D from measurements of O atoms in oxidation of H_2 and D_2 by N_2O, J. Chem. Phys. 76 (1982) 311–315.
[33] N. Cohen, Are reaction rate coefficients additive? Revised transition state theory calculations for OH + alkane reactions, Int. J. Chem. Kinet. 23 (1991) 397–417.
[34] L.A. Curtiss, P.C. Redfern, K. Raghavachari, Gaussian-4 theory, J. Chem. Phys. 126 (2007) 084108.
[35] M.J. Frisch, G.W. Trucks, H.B. Schlegel, G.E. Scuseria, M.A. Robb, J.R. Cheeseman, G. Scalmani, V. Barone, G.A. Petersson, H. Nakatsuji, X. Li, M. Caricato, A.V. Marenich, J. Bloino, B.G. Janesko, R. Gomperts, B. Mennucci, H.P. Hratchian, J.V. Ortiz, A.F. Izmaylov, J.L. Sonnenberg, Williams, F. Ding, F. Lipparini, F. Egidi, J. Goings, B. Peng, A. Petrone, T. Henderson, D. Ranasinghe, V.G. Zakrzewski, J. Gao, N. Rega, G. Zheng, W. Liang, M. Hada, M. Ehara, K. Toyota, R. Fukuda, J. Hasegawa, M. Ishida, T. Nakajima, Y. Honda, O. Kitao, H. Nakai, T. Vreven, K. Throssell, J.A. Montgomery Jr., J.E. Peralta, F. Ogliaro, M.J. Bearpark, J.J. Heyd, E.N. Brothers, K.N. Kudin, V.N. Staroverov, T.A. Keith, R. Kobayashi, J. Normand, K. Raghavachari, A.P. Rendell, J.C. Burant, S.S. Iyengar, J. Tomasi, M. Cossi, J.M. Millam, M. Klene, C. Adamo, R. Cammi, J.W. Ochterski, R.L. Martin, K. Morokuma, O. Farkas, J.B. Foresman, D.J. Fox, Gaussian 16 Rev. A.03, Wallingford, CT, 2016.
[36] J.M. Simmie, K.P. Somers, Benchmarking Compound Methods (CBS-QB3, CBS-APNO, G3, G4, W1BD) against the Active Thermochemical Tables: A Litmus Test for Cost-Effective Molecular Formation Enthalpies, J. Phys. Chem. A 119 (2015) 7235–7246.
[37] Active Thermochemical Tables (ATcT) values based on ver. 1.122x of the thermochemical network, Argonne National Laboratory, Lemont, Illinois, 2022, https://doi.org/10.17038/CSE/1885922 available at ATcT.anl.gov.
[38] P. Sela, Y. Zhang, J. Herzler, M. Fikri, C. Schulz, S. Peukert, Pyrolysis of diethyl carbonate: Shock-tube and flow-reactor measurements and modeling, Proc. Combust. Inst. 38 (2021) 987–996.
[39] J. Herzler, S.A. Mujaddadi, M. Fikri, C. Schulz, S. Peukert, Single-pulse shock-tube study on the pyrolysis of small esters (ethyl and propyl propanoate, isopropyl acetate) and methyl isopropyl carbonate, Proc. Combust. Inst. 39 (2023) 49–61.
[40] S. Canneaux, F. Bohr, E. Henon, KiSThelP: A program to predict thermodynamic properties and rate constants from quantum chemistry results, J. Comput. Chem. 35 (2014) 82–93.
[41] R.B. McClurg, R.C. Flagan, W.A. Goddard III, The hindered rotor density-of-states interpolation function, J. Chem. Phys. 106 (1997) 6675–6680.
[42] A.E. Lutz, R.J. Kee, J.A. Miller, SENKIN: A FORTRAN program for predicting homogeneous gas phase chemical kinetics with sensitivity analysis, Sandia National Labs., Livermore, CA (USA), 1988. Report SAND-87-8248.

[43] R.J. Kee, F.M. Rupley, J.A. Miller, M.E. Coltrin, J.F. Grcar, E. Meeks, H.K. Moffat, A.E. Lutz, G.D. Lewis, M.D. Smooke, J. Warnatz, G.H. Evans, R.S. Larson, R.E. Mitchell, L.R. Petzold, W.C. Reynolds, M. Caracotsios, W.E. Stewart, P. Glarborg, C. Wang, O. Adigun, CHEMKIN Collection, Release 3.6, Reaction Design, Inc., San Diego, CA (2000).
[44] M.S. Johnson, M.R. Nimlos, E. Ninnemann, A. Laich, G.M. Fioroni, D. Kang, L. Bu, D. Ranasinghe, S. Khanniche, S.S. Goldsborough, S.S. Vasu, W.H. Green, Oxidation and pyrolysis of methyl propyl ether, Int. J. Chem. Kinet. 53 (2021) 915–938.
[45] L. Ackermann, H. Hippler, P. Pagsberg, C. Reihs, J. Troe, Pulse radiolysis, flash-photolysis, and shock wave study of the recombination H + benzyl → toluene at 300 and 1300-1650 K, J. Phys. Chem. 94 (1990) 5247–5251.
[46] J. Herzler, P. Frank, High temperature reactions of phenylacetylene, Ber. Bunsenges. Phys. Chem. 96 (1992) 1333–1338.
[47] S.S. Kumaran, M.C. Su, K.P. Lim, J.V. Michael, The thermal decomposition of C_2H_5I, Proc. Combust. Inst. 26 (1996) 605–611.
[48] A. Kunz, P. Roth, A high temperature study of the reaction $SiH_4+H \rightleftharpoons SiH_3+H_2$, Ber. Bunsenges. Phys. Chem. 102 (1998) 73–78.
[49] G. Friedrichs, D.F. Davidson, R.K. Hanson, Direct measurements of the reaction H + CH_2O → H_2 + HCO behind shock waves by means of Vis–UV detection of formaldehyde, Int. J. Chem. Kinet. 34 (2002) 374–386.
[50] K. Takahashi, O. Yamamoto, T. Inomata, M. Kogoma, Shock-tube studies on the reactions of dimethyl ether with oxygen and hydrogen atoms, Int. J. Chem. Kinet. 39 (2007) 97–108.
[51] T. Bentz, M. Szőri, B. Viskolcz, M. Olzmann, Pyrolysis of ethyl iodide as hydrogen atom source: kinetics and mechanism in the temperature range 950–1200 K, Z. Phys. Chem. 225 (2011) 1117–1128.
[52] E.A. Irdam, J.H. Kiefer, L.B. Harding, A.F. Wagner, The formaldehyde decomposition chain mechanism, Int. J. Chem. Kinet. 25 (1993) 285–303.
[53] T. He, Z. Wang, X. You, H. Liu, Y. Wang, X. Li, X. He, A chemical kinetic mechanism for the low- and intermediate-temperature combustion of polyoxymethylene dimethyl ether 3 (PODE3), Fuel 212 (2018) 223–235.
[54] S. Peukert, P. Yatsenko, M. Fikri, C. Schulz, High-temperature rate constants for the reaction of hydrogen atoms with tetramethoxysilane and reactivity analogies between silanes and oxygenated hydrocarbons, J. Phys. Chem. A 122 (2018) 5289–5298.
[55] E. Hu, Y. Chen, Z. Zhang, J.-Y. Chen, Z. Huang, Ab initio calculation and kinetic modeling study of diethyl ether ignition with application toward a skeletal mechanism for CI engine modeling, Fuel 209 (2017) 509–520.
[56] G.D. Smith, R.L. Jaffe, D.Y. Yoon, Conformational Characteristics of Dimethoxymethane Based upon ab Initio Electronic Structure Calculations, J. Phys. Chem. 98 (1994) 9072–9077.
[57] J.R. Kneisler, N.L. Allinger, Ab initio and density functional theory study of structures and energies for dimethoxymethane as a model for the anomeric effect, J. Comput. Chem. 17 (1996) 757–766.
[58] D.L. Baulch, C.T. Bowman, C.J. Cobos, R.A. Cox, T. Just, J.A. Kerr, M.J. Pilling, D. Stocker, J. Troe, W. Tsang, R.W. Walker, J. Warnatz, Evaluated kinetic data for combustion modeling: supplement II, J. Phys. Chem. Ref. Data 34 (2005) 757–1397.
[59] C.W. Gao, J.W. Allen, W.H. Green, R.H. West, Reaction mechanism generator: automatic construction of chemical kinetic mechanisms, Comput. Phys. Comm. 203 (2016) 212–225.